

Integrated in silico and 3D in vitro model of macrophage migration in response to physical and chemical factors in the tumor microenvironment

Lee, Sharon Wei Ling; Seager, R J; Litvak, Felix; Spill, Fabian; Sieow, Je Lin; Leong, Penny Hweixian; Kumar, Dillip; Tan, Alrina Shin Min; Wong, Siew Cheng; Adriani, Giulia; Zaman, Muhammad Hamid; Kamm, And Roger D

DOI:

[10.1093/intbio/zyaa007](https://doi.org/10.1093/intbio/zyaa007)

License:

None: All rights reserved

Document Version

Peer reviewed version

Citation for published version (Harvard):

Lee, SWL, Seager, RJ, Litvak, F, Spill, F, Sieow, JL, Leong, PH, Kumar, D, Tan, ASM, Wong, SC, Adriani, G, Zaman, MH & Kamm, ARD 2020, 'Integrated *in silico* and 3D *in vitro* model of macrophage migration in response to physical and chemical factors in the tumor microenvironment', *Integrative Biology*, vol. 12, no. 4, zyaa007, pp. 90-108. <https://doi.org/10.1093/intbio/zyaa007>

[Link to publication on Research at Birmingham portal](#)

Publisher Rights Statement:

This is a pre-copyedited, author-produced version of an article accepted for publication in *Integrative Biology* following peer review. The version of record Sharon Wei Ling Lee, R J Seager, Felix Litvak, Fabian Spill, Je Lin Sieow, Penny Hweixian Leong, Dillip Kumar, Alrina Shin Min Tan, Siew Cheng Wong, Giulia Adriani, Muhammad Hamid Zaman, and Roger D Kamm, Integrated in silico and 3D in vitro model of macrophage migration in response to physical and chemical factors in the tumor microenvironment, *Integrative Biology*, vol. 12, no. 4, zyaa007, pp. 90-108, is available online at: <https://academic.oup.com/ib/article/12/4/90/5816011> and <https://doi.org/10.1093/intbio/zyaa007>

General rights

Unless a licence is specified above, all rights (including copyright and moral rights) in this document are retained by the authors and/or the copyright holders. The express permission of the copyright holder must be obtained for any use of this material other than for purposes permitted by law.

- Users may freely distribute the URL that is used to identify this publication.
- Users may download and/or print one copy of the publication from the University of Birmingham research portal for the purpose of private study or non-commercial research.
- User may use extracts from the document in line with the concept of 'fair dealing' under the Copyright, Designs and Patents Act 1988 (?)
- Users may not further distribute the material nor use it for the purposes of commercial gain.

Where a licence is displayed above, please note the terms and conditions of the licence govern your use of this document.

When citing, please reference the published version.

Take down policy

While the University of Birmingham exercises care and attention in making items available there are rare occasions when an item has been uploaded in error or has been deemed to be commercially or otherwise sensitive.

If you believe that this is the case for this document, please contact UBIRA@lists.bham.ac.uk providing details and we will remove access to the work immediately and investigate.

Integrated in silico and 3D in vitro model of macrophage migration in response to physical and chemical factors in the tumor microenvironment

Journal:	<i>Integrative Biology Journal</i>
Manuscript ID	INTBIO-2019-086.R1
Manuscript Type:	Original Article
Date Submitted by the Author:	n/a
Complete List of Authors:	<p>Lee, Sharon; Singapore-MIT Alliance for Research and Technology Centre, BioSystems and Micromechanics; National University of Singapore Faculty of Medicine, Department of Microbiology and Immunology; Singapore Immunology Network, Agency for Science, Technology and Research</p> <p>Seager, R.J.; Boston University, Department of Biomedical Engineering</p> <p>Litvak, Felix; Boston University, Department of Biomedical Engineering</p> <p>Spill, Fabian; Boston University, Department of Biomedical Engineering; Massachusetts Institute of Technology, Department of Mechanical Engineering; University of Birmingham, School of Mathematics</p> <p>Sieow, Je Lin; Singapore Immunology Network, Agency for Science, Technology and Research</p> <p>Penny, Hweixian; Singapore Immunology Network, Agency for Science, Technology and Research</p> <p>Kumar, Dilip; Singapore Immunology Network, Agency for Science, Technology and Research</p> <p>Tan, Alrina; Singapore Immunology Network, Agency for Science, Technology and Research</p> <p>Wong, Siew Cheng; Singapore Immunology Network, Agency for Science, Technology and Research; National University of Singapore Faculty of Medicine, Department of Microbiology and Immunology</p> <p>Adriani, Giulia; Singapore Immunology Network, Agency for Science, Technology and Research</p> <p>Zaman, Muhammad; Boston University, Department of Biomedical Engineering; Boston University, Howard Hughes Medical Institute</p> <p>Kamm, Roger; Massachusetts Institute of Technology, Department of Mechanical Engineering; Massachusetts Institute of Technology, Department of Biological Engineering</p>
Keywords:	Macrophages, Interstitial flow, Tumor microenvironment, Microfluidic cancer models, 3D cell migration, Cell signaling analysis

SCHOLARONE™
Manuscripts

Integrated *in silico* and 3D *in vitro* model of macrophage migration in response to physical and chemical factors in the tumor microenvironment

Lee, Sharon Wei Ling^{1,2,3,+}, Seager, R.J.^{4,+}, Litvak, Felix⁴, Spill, Fabian^{4,5,6}, Sieow, Je Lin³, Penny, Hweixian Leong³, Kumar, Dillip³, Tan, Alrina Shin Min³, Wong, Siew Cheng^{2,3}, Adriani, Giulia^{3,*}, Zaman, Muhammad Hamid^{4,7,*}, Kamm, Roger Dale^{5,8,*}

- ¹ BioSystems and Micromechanics IRG, Singapore-MIT Alliance for Research and Technology, Singapore, 138602, Singapore
- ² Department of Microbiology and Immunology, Yong Loo Lin School of Medicine, National University of Singapore (NUS), Singapore, 117597, Singapore
- ³ Singapore Immunology Network (SIgN), Agency for Science, Technology, and Research (A*STAR), Singapore
- ⁴ Department of Biomedical Engineering, Boston University, Boston, MA, 02215, USA
- ⁵ Department of Mechanical Engineering, Massachusetts Institute of Technology, Cambridge, MA, 02139, USA
- ⁶ School of Mathematics, University of Birmingham, Birmingham, B15 2TT, UK
- ⁷ Howard Hughes Medical Institute, Boston University, Boston, MA, 02215, USA
- ⁸ Department of Biological Engineering, Massachusetts Institute of Technology, Cambridge, MA, 02139, USA

+ These authors contributed equally to the work.

* Corresponding authors.

Roger Dale Kamm, Email: rdkamm@mit.edu
Muhammed Hamid Zaman, Email: zaman@bu.edu
Giulia Adriani, Email: giulia_adriani@immunol.a-star.edu.sg

Abstract

Macrophages are abundant in the tumor microenvironment (TME), serving as accomplices to cancer cells for their invasion. Studies have explored the biochemical mechanisms that drive pro-tumor macrophage functions, however the role of TME interstitial flow (IF) is often disregarded. Therefore, we developed a three-dimensional microfluidic-based model with tumor cells and macrophages to study how IF affects macrophage migration and its potential contribution to cancer invasion. The presence of either tumor cells or IF individually increased macrophage migration directedness and speed. Interestingly, there was no additive effect on macrophage migration directedness and speed under the simultaneous presence of tumor cells and IF. Further, we present an *in silico* model that couples chemokine-mediated signaling with mechanosensing networks to explain our *in vitro* observations. In our model design, we propose IL-8, CCL2 and β -integrin as key pathways that commonly regulate various Rho GTPases. In agreement, *in vitro* macrophage migration remained elevated when exposed to a saturating concentration of recombinant IL-8 or CCL2, or to the co-addition of a sub-saturating concentration of both cytokines. Moreover, antibody blockade against IL-8 and/or CCL2 inhibited migration that could be restored by IF, indicating cytokine-independent mechanisms of migration induction. Importantly, we demonstrate the utility of an integrated *in silico* and 3D *in vitro* approach to aid the design of tumor-associated macrophage-based immunotherapeutic strategies.

Insight

Macrophages and interstitial flow (IF) have emerged as important characteristics of the complex tumor microenvironment (TME). However, little is understood about the interactions of these variables. Therefore, we developed an integrated mathematical-experimental approach to probe the interplay of tumor cells, macrophages and IF. The experiments utilize a novel three-dimensional microfluidic *in-vitro* model where tumor cells can be co-cultured with primary macrophages with IF present. Employing this platform and our mathematical model, we show how key tumor-secreted factors (TSF) and IF are integrated by

macrophages, which consequently migrate with increased directedness and speed, thus enhancing potential interactions with cancer cells to support their invasiveness. Therefore, we deduce that IF, additionally or complementary to TSF, importantly drives macrophage migration in the TME.

INTRODUCTION

Interstitial flow (IF) is an important, yet underappreciated, biophysical force that drives cancer progression [1]. It is derived from an elevated interstitial fluid pressure (IFP) in the solid tumor (~ 10-40 mmHg) [2,3], due to highly permeable tumor vessels and the lack of functional lymphatic vessels [4,5]. This abnormal pressure results in a steep pressure gradient near the tumor margin with escape of interstitial fluid from the tumor mass into the surrounding tissues [6–8], where IFP then drops rapidly to normal tissue values (~ 0 mmHg) [4,9]. Because this fluid contains tumor-secreted cytokines and growth factors and can influence tumor cell migration, IF essentially fuels tumor metastasis [9,10].

Clinical data across different solid cancers have shown that higher IFP at the tumor site strongly correlates with poorer patient survival [11–14]. Accordingly, IFP has been viewed as a strong prognostic factor that is independent of other clinical parameters [11,15], with ongoing effort to develop strategies to decrease IFP, and hence IF, in patients [16–21]. However, given the complexity of cancer pathology, current findings have only begun to explain the multiple interacting facets of IF’s role in cancer, including its regulation of pivotal immune cell players in the tumor microenvironment (TME). This scenario motivates the need for additional studies that investigate the role of IF on multiple cell types in the TME.

Macrophages are highly abundant at the tumor-stromal boundary [22–24], where there are high levels of IF [25,26]. Interestingly, this is also where there are high rates of tumor cell invasion [25,26]. Clinical and experimental evidence report that macrophages crucially support tumor metastasis [27], with a meta-analysis showing that over 80% of studies correlate poor patient outcomes and macrophage density [28]. Moreover, intravital imaging of fluorescently labelled cells in mammary tumors has shown that tumor cells

and macrophages move concordantly [24]. Indeed, growing evidence suggests that macrophages could be importantly involved in IF-based tumor cell invasion [25,29]. Therefore, interfering with the signaling pathways associated with IF, tumor cells and macrophages could potentially inhibit the pro-tumor function of macrophages and also tumor cell metastasis [30].

Macrophages remodel extracellular matrix (ECM) through matrix metalloproteinases (MMP) which degrade collagen and create tracks for tumor cells to migrate [31,32]. Such tracks also enable macrophages to migrate toward and interact with other cells in the TME to support tumor progression, for example by their contact-dependent support of the epithelial-to-mesenchymal transition (EMT) of tumor cell aggregates [33], or their contact with the endothelium to increase its permeability to intravasating tumor cells [34]. Therefore, macrophage migration in the TME is an important parameter that reflects their ability to support tumor cell invasion through the ECM in the process of metastasis [35]. Current understanding of macrophage migration has been confined to the regulation by biological cues in the TME, including tumor-secreted factors (TSF) which have been identified as key regulators of macrophage motility [36–40].

The study of cell migration requires suitable experimental models that allow cells to migrate with spatial and temporal freedom, while allowing for real-time measurements. A classical set-up is the transwell migration assay, where cell motility is assessed by the number of cells that migrate across a two-dimensional (2D) porous membrane between upper and lower chambers [41,42]. While the use of such platforms contributes insight toward cell motility, they lack a 3D ECM and fail to accurately mimic the physiological setting [43,44]. Specifically, recent studies have reported differences in protein expression when cells migrate through a 3D matrix compared to their migration on a 2D substrate [42,44–46]. For example, focal adhesion kinase (FAK) is crucial for migration through a 3D matrix, but in 2D, FAK-null cells can compensate for migration defects by over-expressing other cell migration machineries [46]. Moreover, matrix degradation, an important factor in 3D migration, is not required for migration on a 2D surface. Indeed, there is evidence that 3D measurements of migration directedness (ability to maintain direction of motion) and speed do not correlate with migration in 2D [45]. Finally, these classical assays

1
2
3 99 present end-point readouts of the number of transmigrated cells, failing to capture the temporal dynamics
4
5 100 of cell motility.
6
7
8 101 On the other hand, microfluidic models present suitable 3D environments for real-time measurements of
9
10 102 migration directedness and speed. However, current microfluidic models of IF comprise a gel-based mono-
11
12 103 culture of cells including tumor cells [47,48], fibroblasts [49,50] or macrophages [51]. The most cellularly
13
14 104 complex model has tumor cells seeded in a central microchannel with an additional endothelial monolayer
15
16 105 in the adjacent microchannel [52]. Recently, Li *et al.* report evidence that IF increased the migration
17
18 106 directedness and speed of mouse macrophages using a single-gel microfluidic platform [51]. However,
19
20 107 there remains open questions such as how IF which specifically arises from tumor cells can dynamically
21
22 108 modulate macrophage migration, and whether IF or TSF is the stronger determinant of macrophage
23
24 109 migration behavior. To this end, the *in silico* modeling of *in vitro* data can yield quantitative insight into
25
26 110 the biological signaling and biomechanics of macrophage migration in a 3D TME setting [53,54].
27
28
29
30 111 The present work seeks to address the effect of tumor-derived IF and TSF on macrophage migration by
31
32 112 developing a human-based microfluidic model comprising a co-culture of tumor cells and primary
33
34 113 monocyte-derived macrophages, designed to impart the effect of tumor-derived IF and TSF on
35
36 114 macrophages. Specifically, we will contribute insight toward the dynamic IF-associated interplay that exists
37
38 115 between tumor cells and macrophages. Further, we will clarify if IF and TSF are functionally redundant or
39
40 116 additive in regulating macrophage migration, thus identifying their relative importance as potential
41
42 117 therapeutic targets. Moreover, we explore how our *in vitro* data contributes toward the development of a
43
44 118 refined *in silico* signaling network model that associates TSF, IF and the migration activity of macrophages.
45
46
47 119
48
49
50
51
52
53
54
55
56
57
58
59
60

MATERIALS AND METHODS

Generation and culture of GFP stable cell lines

A human pancreatic adenocarcinoma (PDAC) cell line, Panc1 (ATCC® CRL-1469), and normal pancreatic epithelial cell line hTERT-HPNE (“HPNE”) (ATCC® CRL-4023) were transfected to stably express green fluorescent protein (GFP). GFP gene was amplified from pGreenPuro shRNA Cloning and Expression Lentivector (CMV; System biosciences, SI505A-1) and sub-cloned into ITR-CAG-DEST-IRES-Neomycin-ITR plasmid (generous gift from Marc Supprian Schmidt). ITR-CAG-DEST-IRES-Neomycin-ITR (control plasmid) (Supplementary Fig. S1a) or ITR-CAG-GFP-IRES-Neomycin-ITR (GFP plasmid) (Supplementary Fig. S1b) was mixed with SB100x transposase (1:1 ratio) and the mixture was transiently transfected into the cell line using Lipofectamine 2000 (Thermo Fisher Scientific, 11668027). Three days post-transfection, transfected cells were selected with 300 µg/mL G418 for 10 days. To validate the stable and constitutive expression of GFP, selected cells were analyzed by flow-cytometry. GFP-expressing Panc1 and HPNE were cultured in Iscove’s Modified Dulbecco’s Media (IMDM; GE Healthcare Hyclone, SH30228.01) supplemented with 5% human serum (Innovative Research, IPLA-SER) and 1% 1X Penicillin-Streptomycin (hereafter referred to as “cIMDM”). Cells were maintained in a humidified CO₂ incubator at 37 °C and 5% CO₂.

Multiplex array

Conditioned media were generated from either the 2D culture of Panc1 and HPNE cells using a previously described method [55] or the 3D culture of these cell lines. Briefly, in the 2D culture, 1×10^6 cells were seeded in 30 mL of cIMDM in a T175 flask and allowed to grow to 70-80% confluency. Media were then removed from the flasks, centrifuged for 10 min at 15000 rpm, sterile filtered (0.2 µm pore size) and stored at -20 °C until use. For the 3D culture, cells were seeded at equal densities in the microfluidic device for at least 24 h, before collecting media from all media reservoirs of each device. Cell media were centrifuged at 14000 rpm for 10 min at 4 °C and all supernatants were stored in -20 °C until use. 2D and 3D culture

1
2
3 144 media cytokines were respectively analyzed by the Proteome Profiler™ antibody array (R&D Systems) and
4
5 145 the Milliplex 38 Cytokine kit (Millipore, HCYTMAG-60K-PX38).
6
7

8 146 **Isolation of monocytes and differentiation into macrophages**
9

10
11 147 Blood samples and procedures used in this study have been approved by the Centralized Institutional
12
13 148 Review Board, SingHealth (reference no: 2017/2512) and the Committee on the Use of Humans as
14
15 149 Experimental Subjects (COUHES). All protocols are in accordance with The Code of Ethics of the World
16
17 150 Medical Association. Written informed consent was given according to the principles expressed in the
18
19 151 Declaration of Helsinki. Peripheral blood mononuclear cells (PBMCs) were isolated from whole blood of
20
21 152 healthy donors by Ficoll-Paque (GE Healthcare, 17-1440-02) density gradient centrifugation, and
22
23 153 monocytes were positively isolated using CD14 microbeads (Miltenyi Biotec, Auburn, CA). Monocytes
24
25 154 were maintained in Petri dishes in cIMDM and 100 ng/mL recombinant human M-CSF (Immunotools,
26
27 155 Friesoythe, Germany) over 7 days to generate macrophages. Cell viability was assessed by Trypan blue
28
29
30 156 exclusion and was consistently > 90% viable.
31

32 157 **Fabrication of microfluidic device**
33
34

35 158 Microfluidic devices were fabricated following previously reported protocols [56,57].
36
37 159 Polydimethylsiloxane (PDMS; Sylgard 184 silicone elastomer kit, Dow Corning, Midland, MI, USA) were
38
39 160 fabricated by standard soft lithography methods from a patterned SU-8 silicon wafer. Silicone elastomer
40
41 161 and curing agent were mixed at a 10:1 weight ratio, degassed in a desiccator, poured onto the
42
43 162 photolithographically patterned SU-8 structures and cured overnight at 37 °C. Devices were cut from the
44
45 163 PDMS replica, and inlet and outlet ports were created by biopsy punches before autoclave sterilization.
46
47 164 After drying the devices overnight at 80 °C, PDMS layers were plasma bonded to the glass cover slips to
48
49 165 create channels of approximately 190 μm in height. Each device consists of four connected channels (4.36
50
51 166 mm in length), with two for injecting hydrogels (580 μm wide) and two for culture media (920 μm wide)
52
53
54
55
56
57
58
59
60

(Fig. 1a). Each gel channel contains 9 trapezoidal structures (base lengths of 290 μm and 120 μm , height of 140 μm) [33,55,56].

Cell seeding

All channels were coated with 1 mg/mL poly-D-lysine (PDL) solution (Sigma-Aldrich, St. Louis, MO) to prevent the detachment of collagen gels from the channel walls and left at 80 °C for at least 24 h to restore hydrophobicity [43]. GFP-Panc1 were trypsinized, counted and resuspended in 2.5 mg/mL type I rat tail collagen gel (354236, Corning) solution. Macrophages were harvested by rinsing with D-PBS, incubating with PBS/EDTA (PBS; 2 mM EDTA; Axil Scientific, BUF-1052) for 10–15 min at 37 °C, 5% CO₂, before adding cIMDM and gently scraping. Harvested macrophages were fluorescently stained with 2 μM Cell Tracker Orange, CMRA (Invitrogen) and resuspended separately in the same type of hydrogel. Cell seeding was performed using a protocol that was previously described [33,55,56]. Briefly, the GFP-Panc1 hydrogel suspension was injected into one gel channel and allowed to polymerize for 20 min in the incubator (37 °C, 5% CO₂), followed by injection of the macrophage hydrogel suspension in the other gel channel and then gentle addition of cIMDM into the lateral fluidic channel adjacent to the GFP-Panc1 gel channel. The device was returned to the incubator for 40 min for the second injected hydrogel to polymerize before gentle addition of cIMDM to the media channel adjacent to the macrophage gel channel (Fig. 1b). In some devices, collagen hydrogel without GFP-Panc1 (herein referred to as “blank hydrogel”) was used as the first hydrogel being injected (Fig. 1c). Devices containing cells were left to stabilize overnight in the incubator.

3D assay and quantification of macrophage migration

After overnight incubation, the cell-containing PDMS chamber was sealed against another PDMS layer that contained a large media reservoir (Fig. 1a). To achieve a flow velocity of $\sim 3 \mu\text{m/s}$ through the 3D collagen hydrogel, a media-height difference of 2.5 mm was established at the inlet ports connecting the media reservoir with the channels containing GFP-Panc1 or blank hydrogel. Through this set-up, media flowed from the media reservoir, through the GFP-Panc1 cells (or blank hydrogel), and then finally to the

1
2
3 191 macrophages. Darcy’s law was used to calculate the required media-height difference across the gel
4
5 192 channels (refer to ‘Calculation and verification of interstitial flow’). In some devices, respective
6
7 193 concentrations (ranging from 25 ng/mL to 100 ng/mL) of recombinant human IL-8 (Biolegend, 715404)
8
9 194 and/or recombinant human CCL2 (Peprotech, 300-04) reconstituted in cIMDM was added. In other devices,
10
11 195 0.4 µg/mL of anti-IL-8 antibody (R&D, MAB208) and/or 1 µg/mL of anti-CCL2 antibody (R&D,
12
13 196 MAB279) was added.

15
16 197 Devices were transferred onto a confocal microscope (Olympus model FV1000) fit with a humidified
17
18 198 environmental chamber which maintained a temperature of 37 °C and 5% CO₂. Macrophages were exposed
19
20 199 for 24 h to the various stimuli, including IF, recombinant cytokines and anti-IL-8/anti-CCL2 antibodies,
21
22 200 where their migration in 3D was tracked by time-lapse confocal microscopy, with 3D image stacks taken
23
24 201 every 25 min at a 20X magnification (800 × 800 pixel density). As the cross-sectional area of the reservoirs
25
26 202 was approximately 1500 times that of the hydrogel region, there was a negligible decrease in the media-
27
28 203 height difference during the 24 h duration. IMARIS 9.2 was used to track and quantify the migration
29
30 204 directedness and speed of macrophages in 3D and to produce the cell trajectory plots of macrophage
31
32 205 migration.

33
34
35
36 206 **Calculation and verification of interstitial flow**

37
38
39 207 The hydraulic permeability, K , of the 2.5 mg/mL collagen gel used in this study was previously determined
40
41 208 by Darcy’s law to be $\sim 7 \times 10^{-14} \text{ m}^2$ [51]. Darcy’s law was also used to determine the media-height difference
42
43 209 that was required to establish a desirable IF velocity, v , through the microfluidic device, as represented by
44
45 210 Eq. 1:

46
47
48 211
$$\Delta h = \frac{v\mu W}{K\rho g} \tag{1}$$

49
50

51
52 212 where ρ is the density and μ is the viscosity of cIMDM media, W is the width of the chamber, and Δh is the
53
54 213 initial media–height difference of the reservoir [58]. Based on the geometry of the total hydrogel matrix in

the microfluidic device and the estimated hydraulic permeability, a media–height difference of 2.5 mm was needed to generate an IF velocity of approximately 3 $\mu\text{m/s}$ in the hydrogel.

To quantify and confirm the velocity of IF through the hydrogel at the start and end of the IF treatment, fluorescence recovery after photobleaching (FRAP) was used following a previously reported protocol [59]. Here, 100 $\mu\text{g/mL}$ of 70 kDa FITC-dextran in cIMDM was added and a spot of 30 μm diameter of the hydrogel was bleached using the highest intensity of the laser, according to the microscope guidelines. After the bleaching step, time-lapse images in short intervals (~ 1.6 s) were recorded to monitor the recovery in fluorescence. Photobleaching was performed for the hydrogels in both gel microchannels. ImageJ and Matlab were used to quantify the change in fluorescence after the bleaching step.

Signaling network model construction

A simplified version of the hypothesized signaling network model linking IL-8-based and CCL2-based signaling and IF-induced macrophage migration was constructed by analyzing literature-established signaling pathways associated with each of these extracellular stimuli. Relevant networks were analyzed for intersections (which indicate the presence of key signaling species), and using these intersections, these networks were combined into a single, unified signaling network. Our *in vitro* experimental data showed that similar trends are exhibited by both macrophage migration directedness and speed, suggesting the presence of a common regulator. Moreover, in the absence of a specific molecular output node in our *in vitro* data, we did not model complex downstream signaling and elected to keep the model as simple as possible. As such, we simplified this unified network by removing non-receptor, non-intersecting, intermediate reactions and unifying the various Rho GTPases, that are regulated by the three extracellular stimuli, into a single “common regulator” signaling node. Then, we combined the downstream signaling activity of Rho GTPases into a single regulatory node that regulated both migration directedness and speed.

1
2
3
4
5
6
7
8
9
10
11
12
13
14
15
16
17
18
19
20
21
22
23
24
25
26
27
28
29
30
31
32
33
34
35
36
37
38
39
40
41
42
43
44
45
46
47
48
49
50
51
52
53
54
55
56
57
58
59
60

Mathematical model development

A mathematical model was constructed from the aforementioned hypothesized signaling network model. Specifically, an ordinary differential equation (ODE) model tracked the concentration of each signaling element in its active form and its interactions with other signaling elements [60,61]. The concentrations of activated receptors CXCR1/2 and CCR2 were defined in relation to the concentrations of their respective ligands IL-8 and CCL2 using steady state approximations and the ligand-receptor dissociation constant (Eq. 2 and 3) [62]. The concentration of activated FAK in response to integrin-mediated, IF-induced signaling was calculated using a Hill function. Here, IF speed was correlated with the steady state concentration of activated FAK, and constants were calculated to reproduce *in vitro* experimental observations (Eq. 4) [51]. Next, the concentration of active G proteins dissociating from G protein-coupled receptors CXCR1/2 and CCR2 in response to IL-8 and CCL2 binding, respectively, was calculated by integrating the two receptor signals in an additive manner through Hill functions with corresponding dissociation constants (Eq. 6). Then, we calculated the concentration of active common regulator (Eq. 8). Here, the concentrations of IL-8, FAK, and CCL2 additively contributed to common regulator activation through Hill functions with corresponding dissociation constants. Finally, migration directedness and speed were modeled as Hill functions that exhibit basal activity when no active common regulator is present and increase asymptotically to a maximum value as the concentration of active common regulator increases (Eq. 9 and 10). Table 1 defines the signaling species being tracked by the model.

Table 1. Species variable abbreviations, definitions, initial steady state values and units.

Species	Abbreviation	Definition	Initial Value	Units
S ₁	IL-8	Interleukin-8	9.01*	nM
S ₂	CCL2	C-C motif chemokine ligand 2	9.07*	nM
S ₃	IF	Interstitial flow	3000	nm/s
S ₄	CXCR1/2	C-X-C motif chemokine receptor 1 or 2; receptor for IL-8	0	nM
S ₅	CCR2	C-C chemokine receptor type 2; receptor for CCL2	0	nM
S ₆	FAK	Focal adhesion kinase; activated in response to interstitial flow	9.49	nM
S ₇	G proteins	Family of signaling G proteins (associated with G protein-coupled receptors CXCR1/2 and CCR2)	0	nM
S ₈	Common regulator	Downstream common regulator of migration directedness and speed. Potentially one or more Rho GTPases such as CDC42, Rac1 and/or RhoA	103	nM
M _D	Directedness	Migration directedness relative to control	1.00	-
M _S	Speed	Migration speed relative to control	1.00	-

*Equivalent to 100 ng/mL.

The mathematical modeling framework is as follows (Eq. 2 – 10):

$$S_4 = \frac{S_{4,tot}S_1}{k_1 + S_1} \quad (2)$$

$$S_5 = \frac{S_{5,tot}S_2}{k_2 + S_2} \quad (3)$$

$$S_6 = b_3 + \frac{(S_{6,tot} - b_3)S_3}{k_3 + S_3}, \text{ where } k_3 = S_{3,data} \left(\frac{S_{6,tot} - b_3}{b_3(\delta - 1)} \right) \quad (4)$$

$$S_{7,i} = S_{7,tot} - S_7 \quad (5)$$

$$\frac{dS_7}{dt} = S_{7,i} \left(\frac{p_4 S_4^{n_4}}{k_4^{n_4} + S_4^{n_4}} + \frac{p_5 S_5^{n_5}}{k_5^{n_5} + S_5^{n_5}} \right) - c_7 S_7 \quad (6)$$

$$S_{8,i} = S_{8,tot} - S_8 \quad (7)$$

$$\frac{dS_8}{dt} = S_{8,i} \left(\frac{p_6 S_7^{n_6}}{k_6^{n_6} + S_7^{n_6}} + \frac{p_7 S_6^{n_7}}{k_7^{n_7} + S_6^{n_7}} \right) - c_8 S_8 \quad (8)$$

$$M_D = 1 + (r_D - 1) \frac{S_8^{n_D}}{k_D^{n_D} + S_8^{n_D}} \quad (9)$$

$$M_S = 1 + (r_S - 1) \frac{S_8^{n_S}}{k_S^{n_S} + S_8^{n_S}} \quad (10)$$

To simulate experiments involving the treatment of macrophages with TSF, or co-culture with cancer cells without IF, the following relationship was used to simulate TSF composition (Eq. 11):

$$[CCL2]_{TSF} = r_{TSF} [IL - 8]_{TSF} \quad (11)$$

where $[IL-8]_{TSF}$ and r_{TSF} are free parameters fit to experimental data.

Furthermore, to simulate experiments where TSF-treated macrophages are exposed to anti-IL-8 and/or anti-CCL2 antibodies, the following functions were used to determine the uninhibited concentrations of each cytokine (Eq. 12 and 13):

$$[IL - 8]_{\alpha} = [IL - 8]_{TSF} \left(\frac{k_{\alpha, IL8} [IL - 8]_{TSF}}{\alpha_{IL8} + k_{\alpha, IL8} [IL - 8]_{TSF}} \right) \quad (12)$$

$$[CCL2]_{\alpha} = [CCL2]_{TSF} \left(\frac{k_{\alpha, CCL2} [CCL2]_{TSF}}{\alpha_{CCL2} + k_{\alpha, CCL2} [CCL2]_{TSF}} \right) \quad (13)$$

Model parameter estimation

The mathematical model was implemented as a purpose-constructed code in Python 2.7 and solved at 50,000 time points over 48 h of simulated experimental time *via* the odeint solver found in the scipy.integrate module using the default settings. The model contained 36 parameters, 13 of which were assigned to experimentally derived values taken from the literature (Table 2), 2 of which were assigned based on manufacturer provided protocols for antibody blockade, and 2 of which were directly calculated from *in vitro* directedness and speed data. Here, the kinetics of each upstream interaction between IL-8, CCL2 or IF speed with downstream signaling elements of the model were taken from the literature. Also, initial conditions of each parameter were determined by running the model without the stimuli until it reached steady state. In addition, the total concentration of each intermediate signaling species (assumed

here to be the total concentration of each species at steady state, including both its active and inactive forms) was assigned to a known benchmark value from the literature. The remaining 19 free parameters were fit to our *in vitro* experimental results using a gradient descent least-squares error minimization approach that minimized the error function (Eq. 14):

$$E = \sum_i \left(\frac{M_{D,i} - m_{D,i}}{m_{D,i}} \right)^2 + \sum_i \left(\frac{M_{S,i} - m_{S,i}}{m_{S,i}} \right)^2 \quad (14)$$

where $M_{D,i}$ and $M_{S,i}$ are the simulated migration directedness and speed for each stimulus, respectively, $m_{D,i}$ and $m_{S,i}$ are the experimentally measured migration directedness and speed for each stimulus, respectively. Table 2 shows all model parameters, including those generated from the model fitting process. All free parameters were allowed to fit to any positive value, with the exception of δ , the fold increase in FAK activation associated with IF at a speed of $S_{3,data}$, which was constrained to within 50% of the *in vitro* experimentally observed value [48]. Determining the free parameter values by this approach allowed for an accurate fit that was able to capture the trends across all 58 experimental data points.

Table 2. Parameter values used in simulations. All activation rate constants, dissociation constants, hill coefficients, and basal activation constants are numbered such that they correspond to different signaling pathway reactions. All total species concentrations and degradation rates are numbered such that they correspond to the species numbers detailed in Table 1.

Parameter	Value	Units	Definition	Source
p_4	4.27×10^{-5}	1/s 1/nM	Activation rate constant for CXCR1/2 activating G proteins	Fit to <i>in vitro</i> experimental data
p_5	1.28×10^{-4}	1/s 1/nM	Activation rate constant for CCR2 activating G proteins	Fit to <i>in vitro</i> experimental data
p_6	7.67×10^{-3}	1/s 1/nM	Activation rate constant for G proteins activating common regulator	Fit to <i>in vitro</i> experimental data
p_7	2.32×10^{-3}	1/s 1/nM	Activation rate constant for active FAK activating common regulator	Fit to <i>in vitro</i> experimental data
k_1	1.9	nM	Dissociation constant for IL-8 binding to CXCR1/2	[63]
k_2	0.77	nM	Dissociation constant for CCL2 binding to CCR2	[64]

k_4	410	nM	Apparent dissociation constant for active CXCR1/2 activating G proteins	Fit to <i>in vitro</i> experimental data
k_5	937	nM	Apparent dissociation constant for active CCR2 activating G proteins	Fit to <i>in vitro</i> experimental data
k_6	166	nM	Apparent dissociation constant for G proteins activating common regulator	Fit to <i>in vitro</i> experimental data
k_7	175	nM	Apparent dissociation constant for active FAK activating common regulator	Fit to <i>in vitro</i> experimental data
n_4	1.15	-	Hill coefficient for active CXCR1/2 activating G proteins	Fit to <i>in vitro</i> experimental data
n_5	2.09	-	Hill coefficient for active CCR2 activating G proteins	Fit to <i>in vitro</i> experimental data
n_6	5.60	-	Hill coefficient for G proteins activating common regulator	Fit to <i>in vitro</i> experimental data
n_7	1.38	-	Hill coefficient for active FAK activating common regulator	Fit to <i>in vitro</i> experimental data
b_3	9.49	nM	Basal concentration of active FAK	Fit to <i>in vitro</i> experimental data
$S_{4,tot}$	500	nM	Total concentration of active and inactive CXCR1/2	[65]
$S_{5,tot}$	500	nM	Total concentration of active and inactive CCR2	[65]
$S_{6,tot}$	500	nM	Total concentration of active and inactive FAK	[65]
$S_{7,tot}$	500	nM	Total concentration of active and inactive G proteins	[65]
$S_{8,tot}$	500	nM	Total concentration of active and inactive common regulator	[65]
c_7	1.56×10^{-4}	1/s	Combined degradation and dilution rate for G proteins	[66]
c_8	1.56×10^{-4}	1/s	Combined degradation and dilution rate for common regulator	[66]

$S_{3,data}$	3.00×10^3	nm/s	Interstitial flow (IF) speed associated with δ -fold increased FAK activation	[48]
δ	1.43	-	Fold increase in FAK activation associated with IF at $S_{3,data}$ nm/s	[48]
r_S	3.25	-	Ratio between highest and lowest observed migration speed	Calculated from <i>in vitro</i> experimental data
k_S	131	nM	Half maximum constant for common regulator-induced migration speed	Fit to <i>in vitro</i> experimental data
n_S	8.74	-	Hill coefficient for common regulator-induced migration speed	Fit to <i>in vitro</i> experimental data
r_D	2.95	-	Ratio between highest and lowest observed migration directedness	Calculated from <i>in vitro</i> experimental data
k_D	114	nM	Half maximum constant for common regulator-induced migration directedness	Fit to <i>in vitro</i> experimental data
n_D	10.9	-	Hill coefficient for common regulator-induced migration directedness	Fit to <i>in vitro</i> experimental data
$[IL-8]_{TSF}$	1.12	nM	-	Fit to <i>in vitro</i> experimental data
r_{TSF}	1.18	-	-	Fit to <i>in vitro</i> experimental data
α_{IL8}	2.67	nM	Concentration of anti-IL-8 antibody in antibody blockade experiments	Reflective of <i>in vitro</i> experimental conditions
$k_{\alpha,IL8}$	0.888	-	Molar ratio of antibody to IL-8 required for 50% inhibition	Based on manufacturer supplied datasheet
α_{CCL2}	6.67	nM	Concentration of anti-CCL2 antibody in antibody blockade experiments	Reflective of <i>in vitro</i> experimental conditions
$k_{\alpha,CCL2}$	1.32	-	Molar ratio of antibody to CCL2 required for 50% inhibition	Based on manufacturer supplied datasheet

301

1

2

3302Sensitivity analysis

4

5

6303Stimulus sensitivity analysis was used to quantify the effect of each extracellular stimulus on the

7

8304concentration of active common regulator. Here, the elasticity of the concentration of active common

9

10305regulator was computed for the concentration of each stimulus using the following function (Eq. 15):

11

12

13306
$$\phi_{C,X} = \left| \frac{\Delta\%[\text{Common Regulator}]}{\Delta\%X} \right|$$

14

15

16

17

18

19

20

21

22

23

24

25

26

27

28

29

30

31

32

33

34

35

36

37

38

39

40

41

42

43

44

45

46

47

48

49

50

51

52

53

54

55

56

57

58

59

60

(15)

16307where the denominator represents a 20% change in the stimulus under study (centered at the default stimulus

17

18308value given in Table 1) and the numerator represents the percent change in the concentration of active

19

20309common regulator.

21

22

23310An additional stimulus sensitivity analysis was used to quantify the effect of each extracellular stimulus on

24

25311the quality of the model fit against the *in vitro* experimental data, as quantified by the coefficient of

26

27312determination (R^2) value. This was done in order to determine the effect of changing the magnitude of each

28

29313extracellular stimulus on the migration speed and directedness magnitudes induced by each stimulus

30

31314relative to one another. This could also be conceptualized as quantifying the influence of each extracellular

32

33315stimulus on the trends within the data across all extracellular stimuli. Here, the model R^2 elasticity was

34

35316computed for each stimulus using the following function (Eq. 16):

36

37

38

39

40

41

42

43

44

45

46

47

48

49

50

51

52

53

54

55

56

57

58

59

60

39317
$$\phi_{R,X} = \left| \frac{\Delta\%R^2}{\Delta\%X} \right|$$

40

41

42

43

44

45

46

47

48

49

50

51

52

53

54

55

56

57

58

59

60

(16)

42318where the denominator represents a 20% change in the stimulus under study (centered at the default stimulus

43

44319value given in Table 1) and the numerator represents the percent change in the R^2 value between the model

45

46320outputs and all *in vitro* experimental directedness and speed data.

47

48

49321Parameter sensitivity analysis was used to quantify the effect of each model parameter on the concentration

50

51322of active common regulator. Here, the elasticity of the concentration of active common regulator was

52

53323computed for each parameter using the following function (Eq. 17):

54

55

56

57

58

59

60

$$\phi_{C,P} = \left| \frac{\Delta\%[\text{Common Regulator}]}{\Delta\%P} \right| \quad (17)$$

where the denominator represents a 20% change in the parameter under study (centered at the default parameter value given in Table 2) and the numerator represents the percent change in the concentration of active common regulator.

Finally, an additional parameter sensitivity analysis was used to quantify the effect of each model parameter on the quality of the model fit against *in vitro* experimental data, as quantified by the R^2 value. This was done in order to determine the effect of changing the magnitude of each reaction parameter on the migration speed and directedness magnitudes induced by each stimulus relative to one another. This could also be conceptualized as quantifying the influence of each parameter on the trends within the data across all extracellular stimuli. Here, the model R^2 elasticity was computed for each parameter using the following function (Eq. 18):

$$\phi_{R,P} = \left| \frac{\Delta\%R^2}{\Delta\%P} \right| \quad (18)$$

where the denominator represents a 20% change in the parameter under study (centered at the default parameter value given in Table 2), and the numerator represents the percent change in the R^2 value between the model outputs and all *in vitro* experimental directedness and speed data.

Statistical analysis

Statistical analysis of experimental data was performed using GraphPad Prism 8.2 (GraphPad Software) considering at least two regions of interest (ROIs) in the hydrogel per device. For each *in vitro* experiment, the average migration directedness or speed of macrophages in each ROI (~ 150 macrophages per ROI) was used to generate a data point. To quantify the agreement between the *in vitro* experimental data and the output values of the mathematical model, the R^2 values were calculated for (1) directedness data only, (2) speed data only, and (3) all data together. At each data point, statistical analysis was performed to determine if the population mean predicted by the model would be likely to produce the *in vitro*

experimental data. Data were plotted as the mean \pm standard error of the mean (SEM), where *n.s.* represents not significant, * represents $P \leq 0.05$, ** represents $P \leq 0.01$, *** represents $P \leq 0.001$ and **** represents $P \leq 0.0001$. Statistical significance was determined using a Student's *t*-test or where appropriate, a one-way ANOVA with Holm-Sidak's multiple comparisons test. Only a *P*-value or adjusted *P*-value of ≤ 0.05 was taken as evidence of statistical significance.

RESULTS

Generation of an *in vitro* 3D co-culture model with tumor interstitial flow

Based on previously optimized protocols [51,56], we designed a 3D *in vitro* microfluidic model of tumor IF to specifically study macrophage migration. In this platform, we cultured tumor cells in one channel and macrophages in the adjacent channel, thus allowing us to simulate and study the impact of tumor-originating IF on macrophage migration without the influence of physical cell contact (Fig. 1). In our set-up, we confirmed that the velocity of IF through both gel channels was within the range reported for tumor tissues [25,26]. FRAP analysis revealed a mean IF velocity of $3.9 \pm 0.7 \mu\text{m/s}$ at the beginning of IF exposure and $4.4 \pm 0.5 \mu\text{m/s}$ after 24 h ($P > 0.05$) (Supplementary Fig. S2). These results correspond with the height difference of 2.5 mm between the two media channels which stayed relatively unchanged over the 24 h. Thus, it could be assumed that IF velocity was relatively constant throughout the duration of IF treatment.

Similar effect on macrophage migration by tumor-secreted factors and interstitial flow

In our first set of *in vitro* experiments, we observed that compared to the control macrophage monoculture without IF (Fig. 2ai), 24 h of IF exposure appeared to increase macrophage motility (Fig. 2aii) as shown by the relatively increased spread of their x-y migration path trajectories. Interestingly, it appeared that the presence of tumor cells alone without IF (TSF) also increased the spread of migration path trajectories relatively (Fig. 2aiii), suggesting that either IF or TSF alone could promote increased macrophage motility.

Interestingly, combining IF and TSF (at the cell concentrations tested in Fig. 2) did not have an additive effect on the spread of macrophage migration (Fig. 2aiv).

To ascertain the effect of each stimulus on macrophage motility, we quantified the directedness and speed of macrophage migration during the period of IF exposure following a previously reported approach (Fig. 2b) [36,51]. Consistent with the observed increase in x-y migration path trajectories, IF, TSF or the combination of both could substantially increase the directedness (Fig. 2c) and speed of macrophage migration (Fig. 2d). Compared to the untreated control where the directedness and speed of macrophage migration was $D = 0.31 \pm 0.04$ and $S = 8.3 \pm 1.2 \mu\text{m/h}$, respectively, a 2-fold increase in directedness and 3-fold increase in speed was observed for the conditions of IF ($D = 0.57 \pm 0.03$, $S = 19 \pm 3 \mu\text{m/h}$), TSF ($D = 0.63 \pm 0.04$, $S = 23 \pm 3 \mu\text{m/h}$) and the IF-TSF combination ($D = 0.62 \pm 0.06$, $S = 24 \pm 3 \mu\text{m/h}$), and these values are within the range reported in previous *in vitro* investigations [51].

Hypothesized signaling pathway linking key tumor-secreted factors and Rho GTPase-regulated migration

A multiplex cytokine array of culture supernatant of the tumor cell line (Panc1) and a normal control cell line (HPNE) was conducted to identify the main cytokines within TSF that drove the migration behavior that we observed *in vitro* of macrophages. Our analysis on 2D cell culture-derived supernatant revealed several cytokines secreted at higher levels by the Panc1 compared to the HPNE cell line (Fig. 3a). A review of known signaling networks revealed that the upregulation of CCL2 and IL-8 is highly associated with the regulation of cell migration [67,68]. We also confirmed that Panc1 secreted higher levels of both cytokines than HPNE in the 3D *in vitro* culture environment (Fig. 3b), suggesting that IL-8 and CCL2 could mainly drive the migration we observed of macrophages in the 3D *in vitro* system.

Mechanistically, IL-8 [67,69,70] and CCL2 [68,71–74] bind to G protein-coupled receptors CXCR1/2 and CCR2, respectively, resulting in the activation and subsequent dissociation of an associated G protein [75]. This releases the α subunit of the G protein to activate further intracellular signaling that results in the post-

1
2
3 394 translational regulation of regulatory proteins such as small monomeric GTPases of the Rho-family, leading
4
5 395 to polymerization and retraction of the actin cytoskeleton which are important processes for cells to migrate.
6
7 396 Additionally, our *in vitro* experimental data support previous studies that have demonstrated a synergistic
8
9 397 integration between these receptors, whereby downstream signals are significantly greater in response to
10
11 398 the activation of both receptors than either receptor alone [76]. This synergy has been shown to depend on
12
13 399 the activation of both receptors, suggesting that synergy is the result of intracellular signaling, as opposed
14
15 400 to extracellular cytokine interactions or receptor-receptor associations [76]. Moreover, even in the presence
16
17 401 of both receptors, certain cell types fail to demonstrate this synergy, suggesting this behavior arises from a
18
19 402 characteristic intracellular signaling motif or protein that is unique to certain cell types such as macrophages
20
21 403 [77]. G proteins represent a common element in the downstream signaling networks associated with both
22
23 404 receptors [69,74], and are upstream of migration-regulating Rho GTPases and extracellular signal-regulated
24
25 405 kinases (ERK) (which also exhibit a synergistic activation in response to the activation of both receptors)
26
27 406 [76]. Thus, we hypothesized that a subset of G proteins may represent the integration point and the source
28
29 407 of the synergy between these signaling pathways. In addition, IF-modulated signaling, as mediated by
30
31 408 integrin- β 2 and FAK, is known to drive the activation and downstream migratory activity associated with
32
33 409 Rho GTPases [51,78]. Finally, because our *in vitro* experimental data show that IF and TSF induced a
34
35 410 similar increase in directedness and speed, we hypothesized that IL-8, CCL2 and IF regulate one or more
36
37 411 of the relevant Rho GTPases, namely CDC42, Rac1 and/or RhoA [38–40].
38
39
40
41
42 412 Notably, the purpose of our model is to infer the logical structure of the network that integrates multiple
43
44 413 molecular (IL-8 and CCL2) and mechanical (IF) stimuli, but not the intricate details of interactions
45
46 414 associated with the downstream Rho GTPases. For this reason, we model the Rho GTPases collectively
47
48 415 through a single representative concentration, and hereafter denote this group of signaling species
49
50 416 collectively as “common regulator”. Also, as downstream signaling (connecting Rho GTPase activity to
51
52 417 migration-related processes) becomes increasingly complex, we recognize that there is no need to model
53
54 418 all theoretical details of GTPases signaling. Moreover, the similar trends exhibited by both directedness
55
56
57
58
59
60

and speed in response to all tested stimuli could be explained simply by a common regulator, as opposed to more complex interactions between largely independent signaling pathways. Thus, we depicted directedness and speed as phenomena that are indirectly induced by this common regulator, with intermediate signaling described by respective response functions that depend on the concentration of active common regulator. These considerations led to our proposed signaling network model (Fig. 4) [37].

Effect of varying IL-8, CCL2 and/or interstitial flow on macrophage migration

A second set of *in vitro* experiments were conducted to confirm the central roles of IL-8 and CCL2 proposed in the signaling network model. Compared to the non-treated control, where macrophage migration directedness and speed were $D = 0.35 \pm 0.06$ and $S = 8.4 \pm 1.1 \mu\text{m/h}$, respectively, the exogenous addition of saturating concentrations (100 ng/mL) of only IL-8 ($D = 0.56 \pm 0.03$, $S = 20 \pm 2 \mu\text{m/h}$) or only CCL2 ($D = 0.60 \pm 0.07$, $S = 22 \pm 4 \mu\text{m/h}$) to a macrophage monoculture substantially increased migration directedness and speed (Fig. 5a). These increases were comparable to those obtained by exposing the macrophage monoculture to only IF ($D = 0.61 \pm 0.05$, $S = 23 \pm 4 \mu\text{m/h}$). Moreover, simultaneously exposing macrophages to IF together with either IL-8 ($D = 0.59 \pm 0.01$, $S = 19 \pm 4 \mu\text{m/h}$) or CCL2 ($D = 0.60 \pm 0.08$, $S = 22 \pm 3 \mu\text{m/h}$) did not further increase macrophage migration (Fig. 5a), supporting the notion that IF and TSF can commonly regulate macrophage migration behavior.

Next, macrophages were exposed to sub-saturating concentrations of IL-8 and/or CCL2 to test if the same extent of increase in directedness and speed would be achieved as seen with either (1) a saturating concentration of individual cytokines, or (2) the 3D co-culture of macrophages and tumor cells (TSF). Sub-saturating concentrations of 25 ng/mL of IL-8 and 25 ng/mL of CCL2 were identified based on prior titration experiments (Supplementary Fig. S3a and S3b). While exposure to the sub-saturating concentration of only IL-8 ($D = 0.34 \pm 0.03$, $S = 9.9 \pm 1.3 \mu\text{m/h}$) or only CCL2 ($D = 0.35 \pm 0.08$, $S = 11 \pm 2 \mu\text{m/h}$) did not result in an observable increase in directedness and speed, the combined exposure to sub-saturating concentrations of both cytokines promoted a comparable increase in directedness and speed ($D = 0.54 \pm$

1
2
3 443 0.09, $S = 21 \pm 3 \mu\text{m/h}$) to the TSF condition ($D = 0.6 \pm 0.1$, $S = 22 \pm 2 \mu\text{m/h}$) (Fig. 5b). Importantly, the
4
5 444 data suggest a synergistic integration of the intracellular signals associated with these two cytokines.
6
7
8 445 Finally, the introduction of $0.4 \mu\text{g/mL}$ of anti-IL-8 and $1 \mu\text{g/mL}$ of anti-CCL2 blocking antibodies could
9
10 446 inhibit the TSF-mediated increase in migration directedness and speed (Fig. 5c). Compared to the co-culture
11
12 447 condition (TSF) ($D = 0.56 \pm 0.10$, $S = 25 \pm 2 \mu\text{m/h}$), both directedness and speed were substantially
13
14 448 decreased upon treatment with anti-IL-8 ($D = 0.35 \pm 0.07$, $S = 13.0 \pm 0.3 \mu\text{m/h}$), anti-CCL2 ($D = 0.33 \pm$
15
16 449 0.06 , $S = 13 \pm 1 \mu\text{m/h}$) or combined blockade of both cytokines ($D = 0.27 \pm 0.02$, $S = 11 \pm 1 \mu\text{m/h}$).
17
18 450 Interestingly, IF could restore migration back to a level that was comparable to the TSF condition ($D = 0.47$
19
20 451 ± 0.09 , $S = 21 \pm 2 \mu\text{m/h}$) despite combined antibody blockade of IL-8 and CCL2.
21
22

23 452 **Modeled signaling network captures fundamental migration behaviors**

24
25
26 453 A mathematical model was developed based on the hypothesized signaling network (Fig. 4) using Hill
27
28 454 functions: (1) to relate the concentration of active signaling proteins with the rate of activation of their
29
30 455 downstream targets while capturing various nonlinear signaling behaviors of the system that are not
31
32 456 explicitly modeled (Supplementary Fig. S4), and (2) to determine the steady state concentrations of bound,
33
34 457 active cytokine receptors using dissociation constants from the literature [60,61]. Here, an ODE model
35
36 458 tracked the concentration of each signaling element in its active form and its interactions with other
37
38 459 signaling elements. The mathematical model exhibited similar trends between extracellular stimuli as those
39
40 460 observed in *in vitro* measurements of migration directedness and speed (Fig. 6a-c). Specifically, the addition
41
42 461 of individual or combined stimuli increased directedness and speed to approximately its maximum value,
43
44 462 similar to *in vitro* observations. Also, the mathematical model results exhibited similar trends as *in vitro*
45
46 463 experimentally observed migration responses to sub-saturating concentrations of IL-8 and/or CCL2 (Fig.
47
48 464 6b), to the antibody blockade of IL-8 and/or CCL2 when tumor cells were present (Fig. 6c), and to the
49
50 465 titration of either cytokine concentration in the absence of IF (Supplementary Fig. S3c and S3d).
51
52 466 Quantifying this model agreement across all data points yields a mean R^2 value of 0.71 for all directedness
53
54
55
56
57
58
59
60

data, 0.92 for all speed data, and 0.85 for all directedness and speed data taken together. Therefore, our model could successfully capture 85% of the variation in the *in vitro* experimental data.

Sensitivity analysis reveals most influential stimuli and parameters

Sensitivity analyses were conducted to identify the most influential extracellular stimuli and reaction parameters that impacted macrophage migration speed and directedness. Specifically, they determined the influence of changing the magnitudes of different stimuli and reaction parameters on the magnitude of the migration speed and directedness response. The analyses also determined the influence of these changes on the measurements of the speed and directedness response to each extracellular stimulus relative to one another.

First, we performed a stimulus sensitivity analysis to quantify the relative influence of each modeled stimulus on the concentration of active common regulator (Eq. 15) (Fig. 7a). Because directedness and speed were both regulated by the common regulator, these analyses captured the influence of each stimulus on both types of migration behaviors. IF had the greatest influence on the concentration of active common regulator, with approximately 1.5 times the influence of IL-8 and approximately 7 times that of CCL2.

Then, a stimulus sensitivity analysis focusing on the R^2 value was conducted to quantify the effect of varying the magnitude of each stimulus on the degree of agreement between the model and *in vitro* experimental data (Eq. 16) (Fig. 7b). This was done in order to determine the influence of each stimulus on the trends in directedness and speed across different stimuli as opposed to the concentration of active common regulator (which determines the magnitudes of directedness and speed). The influence of CCL2 on the R^2 value was over 4 times that of IF, which itself was slightly greater than that of IL-8. This analysis suggests that while IF had the greatest influence on the concentration of active common regulator, CCL2 had the dominant influence on the trends in directedness and speed across different stimuli. Taken together, the considerable difference in the influence of the three modeled extracellular stimuli suggests that each plays a different role in the regulation of the downstream directedness and speed signals.

1
2
3 491 Focusing on the kinetics of individual reactions, a parameter sensitivity analysis was conducted to analyze
4
5 492 how a change in a parameter affected the concentration of active common regulator (Eq. 17) (Fig. 7c).
6
7 493 Additionally, parameters were classified according to their associated signaling protein or motif to assess
8
9 494 the influence of reactions associated with each network element on the overall downstream effect. Results
10
11 495 revealed that parameters associated with common regulator and G protein activation and turnover were in
12
13 496 general the most influential. Among G protein-associated parameters, those governing CCL2-induced G
14
15 497 protein activation (k_5 and n_5) were particularly influential. Other highly influential parameters included $S_{5,tot}$,
16
17 498 which dictates the total concentration of CCL2 receptor CCR2, and two parameters associated with
18
19 499 common regulator activation in response to CCL2 signaling (k_6 and n_6), which were the first and third most
20
21 500 influential parameters, respectively. Overall, this analysis suggests an important role for G protein mediated
22
23 501 signals, especially those driven by CCL2 signaling, in the regulation of the common regulator and thus
24
25 502 migration directedness and speed.
26
27
28

29 503 A second parameter sensitivity analysis was conducted to quantify how varying the magnitude of each
30
31 504 parameter changed the R^2 value between the *in vitro* experimental data and model outputs (Eq. 18) (Fig.
32
33 505 7d). This analysis sought to determine the influence of each parameter on the trends in directedness and
34
35 506 speed across different stimuli as opposed to the concentration of active common regulator. Again,
36
37 507 parameters were classified according to their associated signaling protein or motif. The most influential
38
39 508 parameter was n_7 , the Hill coefficient associated with FAK-induced common regulator activation. Other
40
41 509 parameters associated with common regulator activation and turnover were also among the most influential,
42
43 510 including the second most influential parameter $S_{8,tot}$, the total concentration of common regulator.
44
45 511 Parameters associated with G protein activation and turnover were additional influential parameters,
46
47 512 including $S_{7,tot}$, the total concentration of G proteins, and c_7 , the combined degradation and dilution rate
48
49 513 constant for G proteins. Notably, the third and fourth most influential parameters on the R^2 value were k_5
50
51 514 and r_5 , both of which govern the speed response to common regulator activity. In contrast, among the least
52
53 515 influential parameters were those associated with the directedness response to common regulator activity.
54
55
56
57
58
59
60

The disparate influence between migration speed and directedness on the R^2 value suggests that trends in speed across different environmental conditions are more sensitive to changes in speed regulation, than are trends in directedness sensitive to changes in directedness regulation. Furthermore, this disparate influence between speed- and directedness-associated parameters suggests that migration directedness is more directly driven by the concentration of active common regulator. On the other hand, migration speed, although driven by the concentration of active common regulator, is governed by a more nonlinear processing of that signal. Overall, these analyses suggest that common regulator and G protein activation and turnover play a dominant role in determining the trends across different stimuli and thus the agreement between *in vitro* experimental data and the simulated cell migration behaviors based on the model. Furthermore, the analyses suggest that although speed and directedness are regulated by the concentration of active common regulator, these exhibit very different responses to that signal.

DISCUSSION

IF is an important tumor-associated biophysical factor that contributes toward cancer progression and poor patient survival [1,11–14]. Recent evidence suggests that IF also promotes the pro-tumor M2-polarization and migration activity of macrophages [51]. Moreover, clinical data demonstrate that macrophage density strongly correlates with increased metastasis [27]. Such findings suggest a plausible link between IF, macrophage activity (including their migration) and cancer metastasis, a research area that has not been widely studied [27]. In addition, macrophage migration is driven by tumor-secreted cytokines [36–40], which suggests that IF could act jointly with biochemical cues to affect macrophage migration. In this study, we demonstrate, for the first time, that IF can act in concert with tumor-secreted cytokines or factors (TSF) to regulate macrophage migration through a 3D *in vitro* TME-related ECM.

Previously, Li *et al.* observed that IF-exposed mouse macrophages migrated faster than non-treated control macrophages [51]. Following their work, we were interested to explore the results generated using a co-

1
2
3 540 culture set-up of tumor cells and human primary macrophages, which more closely resembles the dynamic
4
5 541 exchange between these cell types in the *in vivo* human TME. Using a two-gel channel set-up with tumor
6
7 542 cells and macrophages in co-culture in adjacent but separate channels, we could delineate between the
8
9 543 effects of TSF and tumor-originating IF on macrophage migration. We observed that IF-exposed
10
11 544 macrophages migrated faster and with increased directedness than non-treated controls which agrees with
12
13
14 545 Li *et al.*'s work. To our knowledge, our model is the first co-culture system that investigates the role of
15
16 546 tumor IF on immune cell migration.

17
18 547 The Panc1 cell line was used to create the *in vitro* co-culture IF system. Panc1 originates from PDAC which
19
20 548 clinically represents one of the most malignant of cancers with one of the highest death rates [79,80]. PDAC
21
22 549 metastasis correlates with a high macrophage infiltrate [55,81–85]. There are also numerous reports of
23
24 550 cytokines underlying PDAC's aggressive biology [86–89]. Therefore, PDAC seemed an appropriate
25
26 551 cancer-immune model for investigating the effect of macrophage migration in response to PDAC-specific
27
28 552 TSF, where the effect of IF can additionally be assessed. Also, our study integrated *in silico* and *in vitro*
29
30 553 methods, an approach that has been highly effective in deriving insight into cell migration mechanisms [90–
31
32 554 93]. Specifically, we demonstrated that by simulating *in vitro* conditions, an *in silico* signaling network
33
34 555 model could be obtained associating key TSF (specifically IL-8 and CCL2), IF and macrophage migration.
35
36 556 In turn, the *in silico* model predictions were confirmed *in vitro* by adding different concentrations of
37
38 557 exogenous IL-8/CCL2 or blocking antibodies against these cytokines and evaluating macrophage
39
40 558 migration.

41
42
43
44 559 In our study, we first observed that the exposure of macrophages to IF or TSF induced a comparable
45
46 560 increase in their migration directedness and speed. Interestingly, the non-additive effect of combining IF
47
48 561 and TSF suggests that both IF and TSF could commonly regulate downstream macrophage migration when
49
50 562 these stimuli are at saturating levels. Then, through a multiplex cytokine array of tumor-conditioned media,
51
52 563 we identified IL-8 and CCL2 as the most probable cytokines driving the migration activity that we observed
53
54 564 in the 3D *in vitro* system. In PDAC, acquisition of IL-8 and its receptors CXCR1 and CXCR2 on tumor
55
56
57
58
59
60

cells [94,95] and macrophages [96,97] correlates with tumor invasion [98–100] and the metastatic potential of solid tumors in murine models [101–106] and patients [107,108]. Similar to IL-8, the secretion of CCL2 and macrophage expression of its receptor CCR2 has been observed in the tumor tissues of patients with advanced metastasis [109–115]. Moreover, CCR2 blockade in a PDAC mouse model could deplete macrophages from the primary tumor to reduce metastasis [116]. Therefore, we focused on IL-8 and CCL2 in our study by virtue of their important role in regulating macrophage migration and PDAC metastasis. Notably, because IL-8/CCL2 are also implicated in the biology of other cancer types [42,117,118], our present findings can also be generalized to other cancers.

To understand the migration mechanism underlying our *in vitro* observations, we developed an *in silico* signaling network model to associate IL-8, CCL2, IF and macrophage migration. To develop this model, we first referenced key literature describing the intracellular signaling pathways associated with IL-8 and CCL2 [38–40], and studies concerning IF-induced cell migration mechanisms based on these cytokines [51,78,119]. Our findings show that IL-8 [67,69,70] and CCL2 [74,120] activate signaling that results in the post-translational regulation of small monomeric GTPases of the Rho-family, leading to macrophage migration through the polymerization and retraction of the actin cytoskeleton. Specifically, in CCL2 signaling, extracellular chemokine CCL2 binds to and activates the chemokine receptor CCR2 expressed on the cell membranes of macrophages. Subsequently, the C-terminal intracellular domain of CCR2 activates intracellular signaling proteins, including phosphatidylinositol-3-kinase (PI3K), which eventually results in the activation of various Rho GTPases, in particular Rac, regulating cytoskeletal reorganization and cell migration [68,71–73,120]. In the case of IL-8 signaling, extracellular chemokine IL-8 binds to and activates receptor CXCR1/2, activating heterotrimeric small G proteins, $G(\alpha,\beta,\gamma)$, which then promote the activation of Rho GTPases. Notably, other signaling activity downstream of CXCR1/2 and $G(\alpha,\beta,\gamma)$ also activates PI3K and FAK.

In addition, IF triggers a process known as outside-in signaling where it engages multiple extracellular signals to activate cell membrane-bound integrins that then initiate intracellular cytoplasmic signaling

1
2
3 590 [119]. These extracellular signals include the binding of integrins to respective ligands in the ECM, and
4
5 591 various mechanical forces originating from IF including fluid shear stresses. Specifically, each stimuli
6
7 592 induces a conformational change in integrin, activating the cytoplasmic signaling element of the protein
8
9 593 and allowing it to interact with other signaling molecules involved in intracellular signaling cascades [119].
10
11
12 594 Additionally, the activation of integrin activates FAK and Src, stimulating Rho GTPases which drive
13
14 595 macrophage cytoskeletal reorganization and migration [51,78]. Based on these findings, we hypothesized
15
16 596 that IL-8, CCL2 and IF commonly regulate a group of Rho GTPases, including CDC42, Rac1 and/or RhoA
17
18 597 [38–40], and this regulates macrophage migration. Additionally, the similar trends exhibited by both
19
20 598 directedness and speed in response to all tested stimuli could be explained simply by a common regulator,
21
22 599 as opposed to more complex interactions between largely independent signaling pathways. Finally, any
23
24 600 attempt to fully model the highly complex signaling associated with migration regulation (that is
25
26 601 downstream of this common signaling point) might greatly complicate the model with no added insight
27
28 602 about how these signals are integrated. Thus, we depicted directedness and speed as phenomena indirectly
29
30 603 induced by this common regulator, with intermediate signaling described by respective response functions
31
32 604 that depend on the concentration of active common regulator.
33
34
35
36 605 To gain additional insight from our modeling framework, we conducted a number of simulations and model
37
38 606 analyses. We first compared the model results to the trends of directedness and speed that we observed *in*
39
40 607 *vitro* in response to the exposure to various combinations of IL-8, CCL2 and IF in order to determine the
41
42 608 level of agreement between the modeled and experimental results. Quantifying this agreement by
43
44 609 calculating the R^2 value across all modeled directedness and speed data, we determined that the model
45
46 610 successfully accounts for over 85% of the variation in the experimental data. In line with *in vitro*
47
48 611 experimentally observed macrophage migration behaviors, our model also displayed an OR gate-like
49
50 612 behavior, where the exposure to a single stimulus (of biologically consistent magnitude) results in
51
52 613 maximum common regulator activation. We highlight that such behavior is essential for integrating
53
54 614 multiple inputs to produce a stable output regardless of input number. It is also an important, though
55
56
57
58
59
60

conditional, example of redundant signaling where multiple signaling pathways lead to the same downstream effect.

Although TSF contains cytokines in addition to IL-8 and CCL2, the connections between the IL-8, CCL2 and IF-induced, integrin- β 2-mediated, signaling appear to suitably explain the *in vitro* experimentally observed macrophage migration. The relatively dominant role of IL-8 and CCL2 is reflected in a second set of experimental data where *in vitro* antibody blockade of IL-8 and/or CCL2 substantially inhibited the TSF-mediated increase in migration. Moreover, the simultaneous exposure of macrophages to sub-saturating concentrations of both IL-8 and CCL2 was able to achieve a similar effect on migration directedness and speed as their exposure to only TSF. Of note, we recognize that IF and TSF do not appear to act additively in the tumor cell-macrophage co-culture set-up where cytokines are likely to be at saturating levels (confirmed by the similar increase in directedness/speed between the TSF condition and concentration of 100 ng/mL IL8 or CCL2 that was used to intentionally achieve saturation, Supplementary Fig. S3). Instead, the increase in directedness/speed with either (1) a combination of IL-8 and CCL2 with each cytokine at a sub-saturating level (25 ng/mL) or (2) sub-saturating level of either cytokine with IF suggests that synergies are possible at non-saturating cytokine concentrations. Such synergies have been previously demonstrated experimentally for macrophages, and have been determined to depend on the unimpaired activity of both CXCR1/2 and CCR2 receptors, suggesting the intracellular integration of both cytokine signals as the primary synergistic mechanism [76].

A comparison of model predictions and *in vitro* data of these antibody blockade and sub-saturating concentration experiments further confirms our network architecture and kinetics assumptions. First, consistent with experiments, the behavior with saturating cytokine concentrations was not observed in response to diminished concentrations. Furthermore, by accurately capturing the signaling instigated by intermediate and sub-saturating cytokine concentrations, our model showed that it is not a simple all-or-nothing OR-gate, but a nuanced model that can capture the response across a gradient of stimuli. Second, the model produced simulated migration behaviors that were consistent with the *in vitro* antibody blockade

1
2
3 640 of IL-8 and/or CCL2, reinforcing its capability to simulate experimentally relevant phenomena and capture
4
5 641 intermediate signaling with diminished cytokine concentrations (as quantified by the R^2 values between
6
7 642 modeled and *in vitro* experimental data).
8
9
10 643 We then conducted a number of sensitivity analyses to determine the most influential aspects of the network
11
12 644 on the network response magnitude and the data trends. Stimulus sensitivity analysis revealed that IF was
13
14 645 more influential than either cytokine on the concentration of active common regulator, whereas CCL2 was
15
16 646 the most influential extracellular stimulus on the directedness and speed trends between various
17
18 647 extracellular stimuli (as quantified by the R^2 values between modeled and *in vitro* experimental data).
19
20 648 Parameter sensitivity analysis then revealed that reactions associated with common regulator and G protein
21
22 649 activation and turnover were the most influential on the resulting concentration of active common regulator
23
24 650 as well as the trends between various extracellular stimuli (quantified by the R^2 values between modeled
25
26 651 and *in vitro* experimental data). Reactions associated with CCL2 signaling were also shown to be among
27
28 652 the most influential on the resulting concentration of active common regulator. Additionally, parameters
29
30 653 associated with the migration speed response to the concentration of active common regulator were very
31
32 654 influential on the trends between stimuli, whereas parameters associated with the migration directedness
33
34 655 response were not. This suggests a more nonlinear processing of common regulator signals in the regulation
35
36 656 of migration speed than of directedness. Notably, although the magnitude of IF velocity has significant
37
38 657 influence on the concentration of active common regulator, the parameters associated with IF-induced
39
40 658 signaling were not among the most influential parameters on the concentration of active common regulator.
41
42
43
44 659 Importantly, our findings substantiate the idea that IF contributes to cancer invasiveness through enhancing
45
46 660 macrophage migration. Indeed, as macrophages would have a heightened capacity to migrate through the
47
48 661 3D ECM, there would be increased likelihood for them to interact with and hence support cancer cell
49
50 662 migration in the process of metastasis. The supportive function of macrophages toward cancer metastasis
51
52 663 was previously demonstrated, where media from tumor-conditioned macrophages increased the expression
53
54 664 of EMT genes in a low EMT-score tumor cell line [55]. Moreover, media conditioned from IF-exposed
55
56
57
58
59
60

macrophages could increase the speed of cancer cell migration through a 3D matrix [51], suggesting that IF could support the capability of macrophages to promote tumor cell invasion. These findings support the view that macrophages play a pivotal intermediary role between the stimulus of IF and the output of cancer cell invasion through 3D ECM. Notably, other stromal cells in the TME may also respond to IF and further influence macrophage and/or cancer cell migration. For example, cancer associated fibroblasts (CAFs) can secrete ECM to remodel the TME matrix and this can influence cell migration in the TME [121]. Future studies could therefore incorporate other TME-related cells, such as CAFs, to evaluate their contribution to the relationship between IF and the metastasis process.

Our model was established using cancer cell lines and macrophages derived from the *in vitro* differentiation of blood-isolated monocytes. By incorporating patient-derived tumor explants and autologous macrophages, our platform could potentially facilitate high-throughput preclinical screening of therapies for personalized treatment. For example, a preclinical screen can be performed of single or combined antibody blockade against CCL2, IL-8 and/or β -integrin. Then, the patient-specific response to these interventions can be quantified through measuring macrophage migration across the different treatments. As such, our work potentially forms the basis for developing a companion diagnostic that comes with a biophysical component such as IF for identifying patient responders. In addition, as IF presents a physical barrier to the effective penetration of drugs into deeper regions of the TME, our model could be used to screen and guide the design of therapeutics to optimize their transport efficiency.

Notably, there are some challenges that arise in the implementation of a patient-derived approach, including the optimization of cell culture media for culturing multiple cell types and the fine tuning of the gel matrix composition. However, unlike murine models, microfluidic systems allow for the precise control of spatial, pressure and chemical gradients that can be tailored to the specific application [122,123]. Moreover, although a microfluidic model system may not fully recapitulate human *in vivo* dynamics, it can allow for the creation of a 3D patient-specific environment that is closer to human *in vivo* settings than 2D *in vitro*

1
2
3 689 models. Microfluidic-based screening is also more rapid and less costly compared to utilizing humanized
4
5 690 murine models [122,123].
6
7
8 691 Therefore, our work presents an integrated *in silico*-3D *in vitro* approach to evaluate the effect of IF and
9
10 692 TSF on macrophage migration. Here, we developed a signaling network model identifying key stimuli and
11
12 693 intermediary proteins that drive macrophage migration, thus identifying potential therapeutic targets for
13
14 694 inhibiting macrophage migration (which evidently associates with their capability to support cancer cell
15
16 695 invasion). Importantly, this work contributes toward an improved understanding of the signaling
17
18 696 mechanism associating IF, macrophage motility and cancer metastasis, an area that should be studied more
19
20 697 extensively to improve cancer treatment.
21
22

23 698
24
25
26 699 **Supplementary Material**

27
28 700 Supplementary material is available at INTBIO online.
29
30 701

31
32
33 702 **Author Contributions**

34
35 703 S.L., W.S.C., G.A. and R.K. designed the study and *in vitro* experiments. S.L., G.A. and A.T. conducted *in*
36
37 704 *vitro* experiments. R.S., F.L. and F.S. developed the computational model. R.S. implemented the model and
38
39 705 conducted simulations. D.K. transfected the human cell lines used in the study. S.L. and R.S. analyzed the
40
41 706 results. W.S.C., G.A., M.Z. and R.K. supervised the study and acquired funding. All authors interpreted the
42
43 707 results, reviewed and edited the manuscript.
44
45 708

46
47
48 709 **Disclosures**

49
50 710 The authors declare no competing interests.
51
52 711

Acknowledgements

The authors would like to acknowledge the SIgN Multiplex Analysis of proteins (MAP) platform for performing the multiplex cytokine array and R&D systems for performing the protein array of cell culture supernatant. We also thank Vicsesvari T. (Singapore-MIT Alliance for Research and Technology, SMART) for assisting with fabricating microfluidic devices, Giovanni S. Offeddu (Massachusetts Institute of Technology) and Luca Possenti (Politecnico di Milano) for their guidance on performing FRAP analysis and Ran Li (Massachusetts General Hospital) for providing scientific and technical input.

Funding Support

This work was supported by the National Research Foundation (NRF), Prime Minister's Office, Singapore, under its CREATE program, SMART BioSystems and Micromechanics (BioSyM) IRG [to S.L and R.K.], a core grant to Singapore Immunology Network (SIgN) from Agency for Science, Technology and Research (A*STAR) [to S.L., A.T., D. K., W.S.C. and G.A.], the Biomedical Research Council (BMRC) [IAF 311006 and BMRC transition funds #H16/99/b0/011 to SIgN Immunomonitoring platform], the National Cancer Institute (NCI) [NCI-U01 CA214381-01 to R.K. and NCI-U01 CA177799 to R.S., F.L., M.Z. and R.K.].

References

1. Wirtz D, Konstantopoulos K, Searson PC. 2011 The physics of cancer: The role of physical interactions and mechanical forces in metastasis. *Nat. Rev. Cancer* **11**, 512–522. (doi:10.1038/nrc3080)
2. Stylianopoulos T, Munn LL, Jain RK. 2018 Reengineering the physical microenvironment of tumors to improve drug delivery and efficacy: From mathematical modeling to bench to bedside. *Trends in Cancer* **4**, 292–319. (doi:10.1016/j.trecan.2018.02.005)
3. K Jain R, Jain RK. 2012 Delivery of molecular and cellular medicine to solid tumors. *Adv. Drug*

1
2
3 737 *Deliv. Rev.* **64**, 353–365. (doi:10.1016/j.addr.2012.09.011)
4
5
6 738 4. Jain RK. 1994 Barriers to drug delivery in solid tumors. *Sci. Am.* **271**, 58–65.
7
8 739 (doi:10.2307/24942767)
9
10
11 740 5. Padera TP *et al.* 2002 Lymphatic metastasis in the absence of functional intratumor lymphatics.
12
13 741 *Science* **296**, 1883–1886. (doi:10.1126/science.1071420)
14
15
16 742 6. Baxter LT, Jain RK. 1989 Transport of fluid and macromolecules in tumors. I. Role of interstitial
17
18 743 pressure and convection. *Microvasc. Res.* **37**, 77–104.
19
20
21 744 7. Baxter LT, Jain RK. 1991 Transport of fluid and macromolecules in tumors. IV. A microscopic
22
23 745 model of the perivascular distribution. *Microvasc. Res.* **41**, 252–272.
24
25
26 746 8. Jain RK, Baxter LT. 1988 Mechanisms of heterogeneous distribution of monoclonal antibodies
27
28 747 and other macromolecules in tumors: Significance of elevated interstitial pressure. *Cancer Res.* **48**,
29
30 748 7022–7032.
31
32
33 749 9. Jain RK, Tong RT, Munn LL. 2007 Effect of vascular normalization by antiangiogenic therapy on
34
35 750 interstitial hypertension, peritumor edema, and lymphatic metastasis: insights from a mathematical
36
37 751 model. *Cancer Res.* **67**, 2729–2735. (doi:10.1158/0008-5472.CAN-06-4102)
38
39
40 752 10. Lichtenbeld HC, Yuan F, Michel CC, Jain RK. 1996 Perfusion of single tumor microvessels:
41
42 753 Application to vascular permeability measurement. *Microcirculation* **3**, 349–357.
43
44 754 (doi:10.3109/10739689609148307)
45
46
47 755 11. Milosevic M, Fyles A, Hedley D, Pintilie M, Levin W, Manchul L, Hill R. 2000 Interstitial fluid
48
49 756 pressure (IFP) predicts disease-free survival independent of clinical prognostic factors in cervix
50
51 757 cancer patients treated with radiotherapy. *Int. J. Radiat. Oncol.* **48**, 135. (doi:10.1016/S0360-
52
53 758 3016(00)80065-6)
54
55
56 759 12. Nathanson SD, Nelson L. 1994 Interstitial fluid pressure in breast cancer, benign breast conditions,

- 760 and breast parenchyma. *Ann. Surg. Oncol.* **1**, 333–338. (doi:10.1007/BF03187139)
- 761 13. Gutmann R, Leunig M, Feyh J, Goetz AE, Messmer K, Kastenbauer E, Jain RK. 1993 Interstitial
762 hypertension in head and neck tumors in patients: Correlation with tumor size. *Cancer Res.* **52**,
763 1993–1995.
- 764 14. Less JR, Posner MC, Boucher Y, Borochoviz D, Wolmark N, Jain RK. 1992 Interstitial
765 hypertension in human breast and colorectal tumors. *Cancer Res.* **52**, 6371–6374.
- 766 15. Roh HD, Boucher Y, Kainicki S, Buchsbaum R, Bloomer WD, Jain RK. 1991 Interstitial
767 hypertension in carcinoma of uterine cervix in patients: Possible correlation with tumor
768 oxygenation and radiation response. *Cancer Res.* **51**, 6695–6698.
- 769 16. Lee C-G *et al.* 2000 Anti-vascular endothelial growth factor treatment augments tumor radiation
770 response under normoxic or hypoxic conditions. *Cancer Res.* **60**, 5565–5570.
- 771 17. Willett CG *et al.* 2004 Direct evidence that the VEGF-specific antibody bevacizumab has
772 antivasular effects in human rectal cancer. *Nat. Med.* **10**, 145–147. (doi:10.1038/nm988)
- 773 18. Lammerts E, Roswall P, Sundberg C, Gotwals PJ, Koteliansky VE, Reed RK, Heldin NE, Rubin
774 K. 2002 Interference with TGF- β 1 and - β 3 in tumor stroma lowers tumor interstitial fluid pressure
775 independently of growth in experimental carcinoma. *Int. J. Cancer* **102**, 453–462.
776 (doi:10.1002/ijc.10722)
- 777 19. Pietras K, Stumm M, Hubert M, Buchdunger E, Rubin K, Heldin C-H, McSheehy P, Wartmann
778 M, Östman A. 2003 STI571 enhances the therapeutic index of epothilone B by a tumor-selective
779 increase of drug uptake. *Clin. Cancer Res.* **9**, 3779–3787.
- 780 20. Salnikov A V *et al.* 2003 Lowering of tumor interstitial fluid pressure specifically augments
781 efficacy of chemotherapy. *Fed. Am. Soc. Exp. Biol.* **17**, 1756–1758. (doi:10.1096/fj.02-1201fje)
- 782 21. Rubin K, Sjöquist M, Gustafsson A-M, Isaksson B, Salvessen G, Reed RK. 2000 Lowering of

- 783 tumoral interstitial fluid pressure by prostaglandin E1 is paralleled by an increased uptake of ^{51}Cr -
 784 EDTA. *Int. J. Cancer* **86**, 636–643. (doi:10.1002/(SICI)1097-0215(20000601)86:5<636::AID-
 785 IJC6>3.0.CO;2-R)
- 786 22. Ohno S, Ohno Y, Suzuki N, Kamei T, Koike K, Inagawa H, Kohchi C, Soma GI, Inoue M. 2004
 787 Correlation of histological localization of tumor-associated macrophages with clinicopathological
 788 features in endometrial cancer. *Anticancer Res.* **24**, 3335–3342.
 789 (doi:10.1016/j.jbankfin.2005.10.009)
- 790 23. Lewis CE, Pollard JW. 2006 Distinct role of macrophages in different tumor microenvironments.
 791 *Cancer Res.* **66**, 605–612. (doi:10.1158/0008-5472.CAN-05-4005)
- 792 24. Wyckoff JB, Wang Y, Lin EY, Li J-F, Goswami S, Stanley ER, Segall JE, Pollard JW, Condeelis
 793 J. 2007 Direct visualization of macrophage-assisted tumor cell intravasation in mammary tumors.
 794 *Cancer Res.* **67**, 2649–56. (doi:10.1158/0008-5472.CAN-06-1823)
- 795 25. Heldin CH, Rubin K, Pietras K, Östman A. 2004 High interstitial fluid pressure - An obstacle in
 796 cancer therapy. *Nat. Rev. Cancer* **4**, 806–813. (doi:10.1038/nrc1456)
- 797 26. Hompland T, Ellingsen C, Øvrebø KM, Rofstad EK. 2012 Interstitial fluid pressure and associated
 798 lymph node metastasis revealed in tumors by dynamic contrast-enhanced MRI. *Cancer Res.* **72**,
 799 4899–4908. (doi:10.1158/0008-5472.CAN-12-0903)
- 800 27. Qian B-Z, Pollard JW. 2010 Macrophage diversity enhances tumor progression and metastasis.
 801 *Cell* **141**, 39–51. (doi:10.1016/j.cell.2010.03.014)
- 802 28. Bingle L, Brown NJ, Lewis CE. 2002 The role of tumour-associated macrophages in tumour
 803 progression: Implications for new anticancer therapies. *J. Pathol.* **196**, 254–265.
 804 (doi:10.1002/path.1027)
- 805 29. Rutkowski JM, Swartz MA. 2006 A driving force for change: Interstitial flow as a

- 806 morphoregulator. *Trends Cell Biol.* **17**, 44–50. (doi:10.1016/j.tcb.2006.11.007)
- 807 30. Wyckoff J *et al.* 2004 A paracrine loop between tumor cells and macrophages is required for
808 tumor cell migration in mammary tumors. *Cancer Res.* **64**, 7022–7029. (doi:10.1158/0008-
809 5472.CAN-04-1449)
- 810 31. Madsen DH *et al.* 2017 Tumor-associated macrophages derived from circulating inflammatory
811 monocytes degrade collagen through cellular uptake. *Cell Rep.* **21**, 3662–3671.
812 (doi:10.1016/j.celrep.2017.12.011)
- 813 32. Opdenakker G, Van Damme J. 1992 Chemotactic factors, passive invasion and metastasis of
814 cancer cells. *Immunol. Today* **13**, 463–464. (doi:10.1016/0167-5699(92)90079-M)
- 815 33. Bai J, Adriani G, Dang TM, Tu T uan, Penny HXL, Wong SC, Kamm RD, Thiery JP. 2015
816 Contact-dependent carcinoma aggregate dispersion by M2a macrophages via ICAM-1 and β 2
817 integrin interactions. *Oncotarget* **6**, 25295–25307. (doi:10.18632/oncotarget.4716)
- 818 34. Zervantonakis IK, Hughes-Alford SK, Charest JL, Condeelis JS, Gertler FB, Kamm RD. 2012
819 Three-dimensional microfluidic model for tumor cell intravasation and endothelial barrier
820 function. *Proc. Natl. Acad. Sci.* **109**, 13515–13520. (doi:10.1073/pnas.1210182109)
- 821 35. Seager RJ, Hajal C, Spill F, Kamm RD, Zaman MH. 2017 Dynamic interplay between tumour,
822 stroma and immune system can drive or prevent tumour progression. *Converg. Sci. Phys. Oncol.* **3**,
823 034002. (doi:10.1088/2057-1739/aa7e86)
- 824 36. Li R, Hebert JD, Lee TA, Xing H, Boussommier-Calleja A, Hynes RO, Lauffenburger DA, Kamm
825 RD. 2016 Macrophage-secreted TNF α and TGF β 1 influence migration speed and persistence of
826 cancer cells in 3D tissue culture via independent pathways. *Cancer Res.* **77**, 279–290.
827 (doi:10.1158/0008-5472.CAN-16-0442)
- 828 37. Ridley AJ. 2001 Rho GTPases and cell migration. *J. Cell Sci.* **114**, 2713–2722.

1
2
3
4
5
6
7
8
9
10
11
12
13
14
15
16
17
18
19
20
21
22
23
24
25
26
27
28
29
30
31
32
33
34
35
36
37
38
39
40
41
42
43
44
45
46
47
48
49
50
51
52
53
54
55
56
57
58
59
60

829 38. Tanaka T, Terada M, Ariyoshi K, Morimoto K. 2010 Monocyte chemoattractant protein-1/CC
830 chemokine ligand 2 enhances apoptotic cell removal by macrophages through Rac1 activation.
831 *Biochem. Biophys. Res. Commun.* **399**, 677–682. (doi:10.1016/j.bbrc.2010.07.141)

832 39. Fan H, Hall P, Santos LL, Gregory JL, Fingerle-Rowson G, Bucala R, Morand EF, Hickey MJ.
833 2011 Macrophage migration inhibitory factor and CD74 regulate macrophage chemotactic
834 responses via MAPK and Rho GTPase. *J. Immunol.* **186**, 4915–4924.
835 (doi:10.4049/jimmunol.1003713)

836 40. Oregioni O, Munro P, Flatau G, Mege J-L, Lemichez E, Landraud L, Boyer L, Doye A. 2004
837 Activation and proteasomal degradation of rho GTPases by cytotoxic necrotizing factor-1 elicit a
838 controlled inflammatory response. *J. Biol. Chem.* **279**, 35849–35857.
839 (doi:10.1074/jbc.m401580200)

840 41. Yamaguchi H, Wyckoff J, Condeelis J. 2005 Cell migration in tumors. *Curr. Opin. Cell Biol.* **17**,
841 559–564. (doi:10.1016/j.ceb.2005.08.002)

842 42. Roussos ET, Condeelis JS, Patsialou A. 2011 Chemotaxis in cancer. *Nat. Rev. Cancer* **11**, 573–
843 587. (doi:10.1038/nrc3078)

844 43. Shin Y, Han S, Jeon JS, Yamamoto K, Zervantonakis IK, Sudo R, Kamm RD, Chung S. 2012
845 Microfluidic assay for simultaneous culture of multiple cell types on surfaces or within hydrogels.
846 *Proc. Natl. Acad. Sci.* **7**, 1247–1259. (doi:10.1038/nprot.2012.051)

847 44. Polacheck WJ, Zervantonakis IK, Kamm RD. 2013 Tumor cell migration in complex
848 microenvironments. *Cell. Mol. Life Sci.* **70**, 1335–1356. (doi:10.1007/s00018-012-1115-1)

849 45. Meyer AS, Hughes-Alford SK, Kay JE, Castillo A, Wells A, Gertler FB, Lauffenburger DA. 2012
850 2D protrusion but not motility predicts growth factor-induced cancer cell migration in 3D
851 collagen. *J. Cell Biol.* **197**, 721–729. (doi:10.1083/jcb.201201003)

- 852 46. Fraley SI, Feng Y, Krishnamurthy R, Kim D-H, Celedon A, Longmore GD, Wirtz D. 2010 A
853 distinctive role for focal adhesion proteins in three-dimensional cell motility. *Nat. Cell Biol.* **12**,
854 598–604. (doi:10.1038/ncb2062)
- 855 47. Tung C, Krupa O, Apaydin E, Liou J-J, Diaz-Santana A, Kim BJ, Wu M. 2013 A contact line
856 pinning based microfluidic platform for modelling physiological flows. *Lab Chip* **13**, 3876.
857 (doi:10.1039/c3lc50489a)
- 858 48. Polacheck WJ, Charest JL, Kamm RD. 2011 Interstitial flow influences direction of tumor cell
859 migration through competing mechanisms. *Proc. Natl. Acad. Sci.* **108**, 11115–11120.
860 (doi:10.1073/pnas.1103581108)
- 861 49. Ng CP, Swartz MA. 2003 Fibroblast alignment under interstitial fluid flow using a novel 3-D
862 tissue culture model. *Am. J. Physiol. - Hear. Circ. Physiol.* **284**, H1771–H1777.
863 (doi:10.1152/ajpheart.01008.2002)
- 864 50. Ng CP, Hinz B, Swartz MA. 2005 Interstitial fluid flow induces myofibroblast differentiation and
865 collagen alignment in vitro. *J. Cell Sci.* **118**, 4731–4739. (doi:10.1242/jcs.02605)
- 866 51. Li R, Serrano JC, Xing H, Lee TA, Azizgolshani H, Zaman M, Kamm RD. 2018 Interstitial flow
867 promotes macrophage polarization toward an M2 phenotype. *Mol. Biol. Cell* **29**, 1927–1940.
868 (doi:10.1091/mbc.E18-03-0164)
- 869 52. Kwak B, Altug O, Shin CS, Park K, Bumsoo H. 2014 Simulation of complex transport of
870 nanoparticles around a tumor using tumor-microenvironment-on-chip. *J. Control. Release* **194**,
871 157–167. (doi:10.1016/j.jconrel.2014.08.027)
- 872 53. Spill F, Bakal C, Mak M. 2018 Mechanical and systems biology of cancer. *Comput. Struct.*
873 *Biotechnol. J.* **16**, 237–245. (doi:10.1016/j.csbj.2018.07.002)
- 874 54. Spill F, Reynolds DS, Kamm RD, Zaman MH. 2016 Impact of the physical microenvironment on

1
2
3 875 tumor progression and metastasis. *Curr. Opin. Biotechnol.* **40**, 41–48.
4
5 876 (doi:10.1016/j.copbio.2016.02.007)
6
7
8 877 55. Penny HL *et al.* 2016 Warburg metabolism in tumor-conditioned macrophages promotes
9
10 878 metastasis in human pancreatic ductal adenocarcinoma. *Oncoimmunology* **5**, 1–15.
11
12 879 (doi:10.1080/2162402X.2016.1191731)
13
14
15 880 56. Adriani G, Ma D, Pavesi A, Kamm RD, Goh ELK. 2017 A 3D neurovascular microfluidic model
16
17 881 consisting of neurons, astrocytes and cerebral endothelial cells as a blood-brain barrier. *Lab Chip*
18
19 882 **17**, 448–459. (doi:10.1039/c6lc00638h)
20
21
22 883 57. Lee SWL, Adriani G, Ceccarello E, Pavesi A, Tan AT, Bertoletti A, Kamm RD, Wong SC. 2018
23
24 884 Characterizing the role of monocytes in T cell cancer immunotherapy using a 3D microfluidic
25
26 885 model. *Front. Immunol.* **9**. (doi:10.3389/fimmu.2018.00416)
27
28
29 886 58. Sudo R, Chung S, Zervantonakis IK, Vickerman V, Toshimitsu Y, Griffith LG, Kamm RD. 2009
30
31 887 Transport-mediated angiogenesis in 3D epithelial coculture. *FASEB J.* **23**, 2155–2164.
32
33 888 (doi:10.1096/fj.08-122820)
34
35
36 889 59. Offeddu GS, Possenti L, Loessberg-Zahl JT, Zunino P, Roberts J, Han X, Hickman D, Knutson
37
38 890 CG, Kamm RD. 2019 Application of transmural flow across in vitro microvasculature enables
39
40 891 direct sampling of interstitial therapeutic molecule distribution. *Small* **1902393**, 1902393.
41
42 892 (doi:10.1002/smll.201902393)
43
44
45 893 60. Ingalls BP. 2013 *Mathematical modeling in systems biology: An introduction*. Cambridge,
46
47 894 Massachusetts.
48
49
50 895 61. Alon U. 2006 *An introduction to systems biology: Design principles of biological circuits*.
51
52 896 Chapman and Hall/CRC.
53
54
55 897 62. Bisswanger H. 2001 *Enzyme Kinetics*. Wiley-VCH.

- 898 63. Suetomi K, Lu Z, Heck T, Wood TG, Prusak DJ, Dunn KJ, Navarro J. 1999 Differential
899 mechanisms of recognition and activation of interleukin-8 receptor subtypes. *J. Biol. Chem.* **274**,
900 11768–11772. (doi:10.1074/jbc.274.17.11768)
- 901 64. Ernst CA, Zhang YJ, Hancock PR, Rutledge BJ, Corless CL, Rollins BJ. 1994 Biochemical and
902 biologic characterization of murine monocyte chemoattractant protein-1. *J. Immunol.* **152**, 3541–
903 3549.
- 904 65. Legewie S, Herzel H, Westerhoff H V, Blüthgen N. 2008 Recurrent design patterns in the
905 feedback regulation of the mammalian signalling network. *Mol. Syst. Biol.* **4**.
906 (doi:10.1038/msb.2008.29)
- 907 66. Eden E, Geva-Zatorsky N, Issaeva I, Cohen A, Dekel E, Danon T, Cohen L, Mayo A, Alon U.
908 2011 Proteome half-life dynamics in living human cells. *Science* **331**, 764–768.
909 (doi:10.1126/science.1199784)
- 910 67. Sham RL, Phatak PD, Ihne TP, Abboud CN, Packman CH. 1993 Signal pathway regulation of
911 interleukin-8-induced actin polymerization in neutrophils. *Blood* **82**, 2546–2551.
- 912 68. Janjanam J, Chandaka GK, Kotla S, Rao GN. 2015 PLC β 3 mediates cortactin interaction with
913 WAVE2 in MCP1-induced actin polymerization and cell migration. *Mol. Biol. Cell* **26**, 4589–
914 4606. (doi:10.1091/mbc.E15-08-0570)
- 915 69. Waugh DJJ, Wilson C. 2008 The interleukin-8 pathway in cancer. *Mol. Pathways* **14**, 6735–6741.
916 (doi:10.1158/1078-0432.CCR-07-4843)
- 917 70. Zhang B *et al.* 2015 Autocrine IL-8 promotes F-actin polymerization and mediate mesenchymal
918 transition via ELMO1-NF- κ B-Snail signaling in glioma. *Cancer Biol. Ther.* **16**, 898–911.
919 (doi:10.1080/15384047.2015.1028702)
- 920 71. Hu Y, Hu X, Boumsell L, Ivashkiv LB. 2008 IFN- γ and STAT1 arrest monocyte migration and

1
2
3 921 modulate RAC/CDC42 pathways. *J. Immunol.* **180**, 8057–65.
4
5 922 (doi:10.4049/jimmunol.180.12.8057)
6
7
8 923 72. Flaishon L *et al.* 2008 Anti-inflammatory effects of an inflammatory chemokine: CCL2 inhibits
9
10 924 lymphocyte homing by modulation of CCL21-triggered integrin-mediated adhesions. *Blood* **112**,
11
12 925 5016–5025. (doi:10.1182/blood-2007-12-129122)
13
14
15 926 73. Fan H, Hall P, Santos LL, Gregory JL, Fingerle-Rowson G, Bucala R, Morand EF, Hickey MJ.
16
17 927 2011 Macrophage migration inhibitory factor and CD74 regulate macrophage chemotactic
18
19 928 responses via MAPK and Rho GTPase. *J. Immunol.* **186**, 4915–4924.
20
21 929 (doi:10.4049/jimmunol.1003713)
22
23
24 930 74. Sagar D *et al.* 2017 Antibody blockade of CLEC12A delays EAE onset and attenuates disease
25
26 931 severity by impairing myeloid cell CNS infiltration and restoring positive immunity. *Sci. Rep.* **7**,
27
28 932 (doi:10.1038/s41598-017-03027-x)
29
30
31 933 75. Wettschureck N, Offermanns S. 2005 Mammalian G Proteins and Their Cell Type Specific
32
33 934 Functions. *Physiol. Rev.* **85**, 1159–1204. (doi:10.1152/physrev.00003.2005)
34
35
36 935 76. Gouwy M, Struyf S, Noppen S, Schutyser E, Springael J-Y, Parmentier M, Proost P, Van Damme
37
38 936 J. 2008 Synergy between coproduced CC and CXC chemokines in monocyte chemotaxis through
39
40 937 receptor-mediated events. *Mol. Pharmacol.* **74**, 485–495. (doi:10.1124/mol.108.045146)
41
42
43 938 77. Arai H, Charo IF. 1996 Differential regulation of G-protein-mediated signaling by chemokine
44
45 939 receptors. *J. Biol. Chem.* **271**, 21814–21819. (doi:10.1074/jbc.271.36.21814)
46
47
48 940 78. Mitra SK, Hanson DA, Schlaepfer DD. 2005 Focal adhesion kinase: In command and control of
49
50 941 cell motility. *Nat. Rev. Mol. Cell Biol.* **6**, 56–68. (doi:10.1038/nrm1549)
51
52
53 942 79. Michalski CW, Weitz J, Büchler MW. 2007 Surgery Insight: Surgical management of pancreatic
54
55 943 cancer. *Nat. Clin. Pract. Oncol.* **4**, 526–535. (doi:10.1038/ncponc0925)
56
57
58
59
60

- 944 80. Deer EL, González-Hernández J, Coursen JD, Shea JE, Ngatia J, Scaife CL, Firpo MA, Mulvihill
945 SJ. 2010 Phenotype and genotype of pancreatic cancer cell lines. *Pancreas* **39**, 425–435.
946 (doi:10.1097/MPA.0b013e3181c15963)
- 947 81. Kurahara H *et al.* 2011 Significance of M2-polarized tumor-associated macrophage in pancreatic
948 cancer. *J. Surg. Res.* **167**, 211–219. (doi:10.1016/j.jss.2009.05.026)
- 949 82. Nywening TM *et al.* 2018 Targeting both tumour-associated CXCR2+ neutrophils and CCR2+
950 macrophages disrupts myeloid recruitment and improves chemotherapeutic responses in pancreatic
951 ductal adenocarcinoma. *Gut* **67**, 1112–1123. (doi:10.1136/gutjnl-2017-313738)
- 952 83. Li N *et al.* 2016 Hypoxia inducible factor 1 (HIF-1) recruits macrophage to activate pancreatic
953 stellate cells in pancreatic ductal adenocarcinoma. *Int. J. Mol. Sci.* **17**, 799.
954 (doi:10.3390/ijms17060799)
- 955 84. Ino Y, Yamazaki-Itoh R, Shimada K, Iwasaki M, Kosuge T, Kanai Y, Hiraoka N. 2013 Immune
956 cell infiltration as an indicator of the immune microenvironment of pancreatic cancer. *Br. J.*
957 *Cancer* **108**, 914. (doi:10.1038/bjc.2013.32)
- 958 85. Candido JB *et al.* 2018 CSF1R+ Macrophages Sustain Pancreatic Tumor Growth through T Cell
959 Suppression and Maintenance of Key Gene Programs that Define the Squamous Subtype. *Cell*
960 *Rep.* **23**, 1448–1460. (doi:10.1016/j.celrep.2018.03.131)
- 961 86. Torres C *et al.* 2015 Prognosis relevance of serum cytokines in pancreatic cancer. *Biomed Res. Int.*
962 (doi:10.1155/2015/518284)
- 963 87. Babic A *et al.* 2018 Plasma inflammatory cytokines and survival of pancreatic cancer patients
964 *Open. Clin. Transl. Gastroenterol.* **9**, 145. (doi:10.1038/s41424-018-0008-5)
- 965 88. Błogowski W, Deskur A, Budkowska M, Sałata D, Madej-Michniewicz A, Dabkowski K, Dołę B,
966 Starzynska T. 2014 Selected cytokines in patients with pancreatic cancer: A preliminary report.

1
2
3
4
5
6
7
8
9
10
11
12
13
14
15
16
17
18
19
20
21
22
23
24
25
26
27
28
29
30
31
32
33
34
35
36
37
38
39
40
41
42
43
44
45
46
47
48
49
50
51
52
53
54
55
56
57
58
59
60

967 *PLoS One* **9**, e97613. (doi:10.1371/journal.pone.0097613)

968 89. Yako YY, Kruger D, Smith M, Brand M. 2016 Cytokines as biomarkers of pancreatic ductal
969 adenocarcinoma: A systematic review. *PLoS One* **11**, 154016. (doi:10.1371/journal.pone.0154016)

970 90. Sun M, Zaman MH. 2017 Modeling, signaling and cytoskeleton dynamics: integrated modeling-
971 experimental frameworks in cell migration. *Wiley Interdiscip. Rev. Syst. Biol. Med.* **9**, 1365.
972 (doi:10.1002/wsbm.1365)

973 91. Kim M-C, Silberberg YR, Abeyaratne R, Kamm RD, Asada HH. 2018 Computational modeling of
974 three-dimensional ECM-rigidity sensing to guide directed cell migration. *Proc. Natl. Acad. Sci.*
975 **115**, E390–E399. (doi:10.1073/pnas.1717230115)

976 92. Mark C, Metzner C, Lautscham L, Strissel PL, Strick R, Fabry B. 2018 Bayesian model selection
977 for complex dynamic systems. *Nat. Commun.* **9**, 1803. (doi:10.1038/s41467-018-04241-5)

978 93. Mak M, Spill F, Kamm RD, Zaman MH. 2016 Single-cell migration in complex
979 microenvironments: Mechanics and aignaling dynamics. *J. Biomech. Eng.* **138**, 021004.
980 (doi:10.1115/1.4032188)

981 94. Murphy C *et al.* 2005 Nonapical and Cytoplasmic Expression of Interleukin-8, CXCR1, and
982 CXCR2 Correlates with Cell Proliferation and Microvessel Density in Prostate Cancer. *Clin*
983 *Cancer Res.* **11**.

984 95. Venkatakrishnan G, Salgia R, Groopman JE. 2000 Chemokine receptors CXCR-1/2 activate
985 mitogen-activated protein kinase via the epidermal growth factor receptor in ovarian cancer cells.
986 *J. Biol. Chem.* **275**, 6868–6875. (doi:10.1074/jbc.275.10.6868)

987 96. Xu H, Lai W, Zhang Y, Liu L, Luo X, Zeng Y, Wu H, Lan Q, Chu Z. 2014 Tumor-associated
988 macrophage-derived IL-6 and IL-8 enhance invasive activity of LoVo cells induced by PRL-3 in a
989 KCNN4 channel-dependent manner. *BMC Cancer* **14**, 330. (doi:10.1186/1471-2407-14-330)

- 990 97. Fu XT *et al.* 2015 Macrophage-secreted IL-8 induces epithelial-mesenchymal transition in
991 hepatocellular carcinoma cells by activating the JAK2/STAT3/Snail pathway. *Int. J. Oncol.* **46**,
992 587–596. (doi:10.3892/ijo.2014.2761)
- 993 98. Araki S, Omori Y, Lyn D, Singh RK, Meinbach DM, Sandman Y, Lokeshwar VB, Lokeshwar BL.
994 2007 Interleukin-8 is a molecular determinant of androgen independence and progression in
995 prostate cancer. *Cancer Res.* **67**, 6854–6862. (doi:10.1158/0008-5472.CAN-07-1162)
- 996 99. Yao C, Lin Y, Chua MS, Ye CS, Bi J, Li W, Zhu YF, Wang SM. 2007 Interleukin-8 modulates
997 growth and invasiveness of estrogen receptor-negative breast cancer cells. *Int. J. Cancer* **121**,
998 1949–1957. (doi:10.1002/ijc.22930)
- 999 100. Lang K, Niggemann B, Zanker KS, Entschladen F. 2002 Signal processing in migrating T24
1000 human bladder carcinoma cells: Role of the autocrine interleukin-8 loop. *Int. J. Cancer* **99**, 673–
1001 680. (doi:10.1002/ijc.10424)
- 1002 101. Huang S, Mills L, Mian B, Tellez C, Mccarty M, Yang X-D, Gudas JM, Bar-Eli M. 2002 Fully
1003 humanized neutralizing antibodies to interleukin-8 (ABX-IL8) inhibit angiogenesis, tumor growth,
1004 and metastasis of human melanoma. *Am. J. Pathol.* **161**, 125–134. (doi:10.1016/S0002-
1005 9440(10)64164-8)
- 1006 102. Shi Q, Abbruzzese JL, Huang S, Fidler IJ, Xiong Q, Xie K. 1999 Constitutive and inducible
1007 interleukin 8 expression by hypoxia and acidosis renders human pancreatic cancer cells more
1008 tumorigenic and metastatic. *Clin Cancer Res* **5**, 3711–3721.
- 1009 103. Inoue K *et al.* 2000 Interleukin 8 expression regulates tumorigenicity and metastases in androgen-
1010 independent prostate cancer. *Clin Cancer Res* **6**, 2104–2119.
- 1011 104. Karashima TF-BMA and M of HBC through the R of I-8 1 *et al.* 2003 Nuclear factor- κ B mediates
1012 angiogenesis and metastasis of human bladder cancer through the regulation of interleukin-8. *Clin*

1
2
3 1013 *Cancer Res* **9**, 2786–2797.
4
5
6 1014 105. Mian BM, Dinney CPN, Bermejo CE, Sweeney P, Tellez C, Yang XD, Gudas JM, McConkey DJ,
7
8 1015 Bar-Eli M. 2003 Fully human anti-interleukin 8 antibody inhibits tumor growth in orthotopic
9
10 1016 bladder cancer xenografts via down-regulation of matrix metalloproteases and nuclear factor-κB.
11
12 1017 *Clin. Cancer Res.* **9**, 3167–3175.
13
14
15 1018 106. Inoue K, Slaton JW, Kim SJ, Perrotte P, Eve BY, Bar-Eli M, Radinsky R, Dinney CPN. 2000
16
17 1019 Interleukin 8 expression regulates tumorigenicity and metastasis in human bladder cancer. *Cancer*
18
19 1020 *Res.* **60**, 2290–2299.
20
21
22 1021 107. Yuan A, Yang P-C, Yu C-J, Chen W-J, Lin F-Y, Kuo S-H, Luh K-T. 2000 nterleukin-8 messenger
23
24 1022 ribonucleic acid expression correlates with tumor progression, tumor angiogenesis, patient
25
26 1023 survival, and timing of relapse in non–small-cell lung cancer. *Am J Respir Crit Care Med* **162**,
27
28 1024 1957–1963. (doi:10.1164/ajrcm.162.5.2002108)
29
30
31 1025 108. Fernando RI, Hamilton DH, Dominguez C, David JM, Mccampbell KK, Palena C. 2016 IL-8
32
33 1026 signaling is involved in resistance of lung carcinoma cells to erlotinib. *Oncotarget* **7**, 42031–
34
35 1027 42044. (doi:10.18632/oncotarget.9662)
36
37
38 1028 109. Mizutani K, Sud S, Mcgregor NA, Martinovski G, Rice BT, Craig MJ, Varsos ZS, Roca H, Pienta
39
40 1029 KJ. 2009 The chemokine CCL2 increases prostate tumor growth and bone metastasis through
41
42 1030 macrophage and osteoclast recruitment. *Neoplasia* **11**, 1235–1242. (doi:10.1593/neo.09988)
43
44
45 1031 110. Loberg RD, Ying C, Craig M, Yan L, Snyder LA, Pienta KJ. 2007 CCL2 as an important mediator
46
47 1032 of prostate cancer growth in vivo through the regulation of macrophage infiltration. *Neoplasia* **9**,
48
49 1033 556–562. (doi:10.1593/neo.07307)
50
51
52 1034 111. Conti I, Rollins BJ. 2004 CCL2 (monocyte chemoattractant protein-1) and cancer. *Semin. Cancer*
53
54 1035 *Biol.* **14**, 149–154. (doi:10.1016/j.semancer.2003.10.009)
55
56
57
58
59
60

- 1036 112. Ueno T, Toi M, Saji H, Muta M, Bando H, Kuroi K, Koike M, Inadera H, Matsushima K. 2000
 1037 Significance of macrophage chemoattractant protein-1 in macrophage recruitment, angiogenesis,
 1038 and survival in human breast cancer. *Clin. Cancer Res.* **6**, 3282–3289.
- 1039 113. Graves DT, Barnhill R, Galanopoulos T, Antoniades HN. 1992 Expression of monocyte
 1040 chemotactic protein-1 in human melanoma in vivo. *Am. J. Pathol.* **140**, 9–14.
- 1041 114. Negus RPM *et al.* 2015 The detection and localization of monocyte chemoattractant protein-1
 1042 (MCP-1) in human ovarian cancer. *J. Clin. Invest.* **95**, 2391–2396. (doi:10.1172/JCI117933)
- 1043 115. Riethdorf L, Riethdorf S, Gutzlaff K, Prall F, Loning T. 1996 Differential Expression of the
 1044 Monocyte Chemoattractant Protein-1 Gene in Human Papillomavirus-16-Infected Squamous
 1045 Intraepithelial Lesions and Squamous Cell Carcinomas of the Cervix Uteri. *Am. J. of Pathology*
 1046 **149**, 1469.
- 1047 116. Sanford DE *et al.* 2013 Inflammatory monocyte mobilization decreases patient survival in
 1048 pancreatic cancer: A role for targeting the CCL2/CCR2 axis. *Clin. Cancer Res.* **19**, 3404–3415.
 1049 (doi:10.1158/1078-0432.CCR-13-0525)
- 1050 117. Vicari AP, Caux C. 2001 Chemokines in cancer. *Cytokine Growth Factor Rev.* **13**, 143–154.
 1051 (doi:10.1016/S1359-6101(01)00033-8)
- 1052 118. Arya M, Patel HRH, Williamson M. 2003 Chemokines: Key players in cancer. *Curr. Med. Res.*
 1053 *Opin.* **19**, 557–564. (doi:10.1185/030079903125002216)
- 1054 119. Shyy JYJ, Chien S. 2002 Role of integrins in endothelial mechanosensing of shear stress. *Circ.*
 1055 *Res.* **91**, 769–775. (doi:10.1161/01.RES.0000038487.19924.18)
- 1056 120. Terashima Y *et al.* 2005 Pivotal function for cytoplasmic protein FROUNT in CCR2-mediated
 1057 monocyte chemotaxis. *Nat. Immunol.* **6**, 827–835. (doi:10.1038/ni1222)
- 1058 121. Joyce JA, Fearon DT. 2015 T cell exclusion, immune privilege and the tumour microenvironment.

1
2
3
4
5
6
7
8
9
10
11
12
13
14
15
16
17
18
19
20
21
22
23
24
25
26
27
28
29
30
31
32
33
34
35
36
37
38
39
40
41
42
43
44
45
46
47
48
49
50
51
52
53
54
55
56
57
58
59
60

1059 *Science* **348**, 74–80. (doi:10.1126/science.aaa6204)

1060 122. Boussommier-Calleja A, Li R, Chen MB, Wong SC, Kamm RD. 2016 Microfluidics: A new tool
1061 for modeling cancer-immune interactions. *Trends in cancer* **2**, 6–19.
1062 (doi:10.1016/j.trecan.2015.12.003)

1063 123. Adriani G, Pavesi A, Tan AT, Bertoletti A, Thierry JP, Kamm RD. 2016 Microfluidic models for
1064 adoptive cell-mediated cancer immunotherapies. *Drug Discov. Today* **21**, 1472–1478.
1065 (doi:10.1016/j.drudis.2016.05.006)

1066

For Review Only

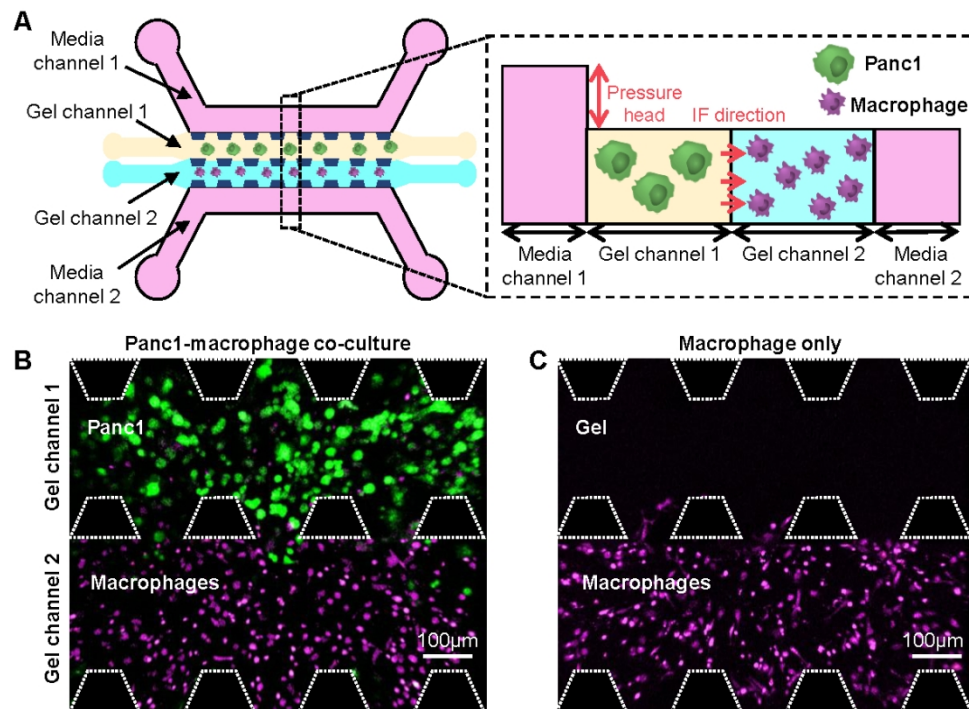


Figure 1. (A) Design of microfluidic co-culture model of tumor cells (Panc1) and macrophages with the incorporation of interstitial flow (IF). Representative confocal image of cell-seeded gel channels at 0 h (B) with tumor cells or (C) without tumor cells.

159x119mm (200 x 200 DPI)

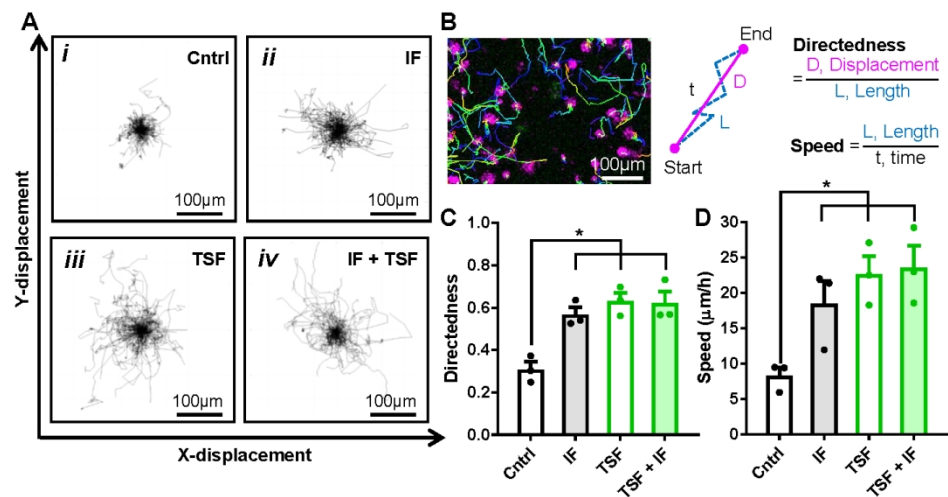


Figure 2. (A) X-Y path trajectories of macrophage migration in the (i) control (Cntrl) monoculture of macrophages without interstitial flow (IF) or exposed to (ii) only IF, (iii) only tumor cells; tumor-secreted factors (TSF), or (iv) both IF and TSF. (B) Quantification method of macrophage migration directedness and speed. (C) Directedness and (D) speed of macrophage migration under the different conditions tested. Data are shown as the mean ± SEM (n = 3), where statistical significance was determined using a one-way ANOVA with Holm-Sidak's multiple comparisons test with * $P \leq 0.05$.

175x88mm (221 x 225 DPI)

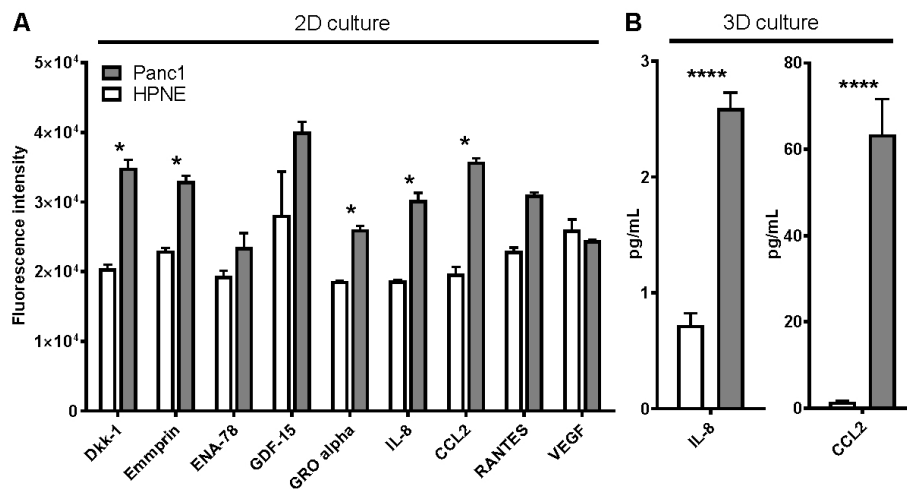


Figure 3. Multiplex array of cytokines in culture supernatant derived (A) from cells grown as a 2D monolayer using the Proteome Profiler™ antibody array (R&D Systems) or (B) from cells grown in a 3D matrix environment using the Milliplex 38 Cytokine kit (Millipore). Data are shown as the mean \pm SEM ($n = 3$), where statistical significance was determined using a Student's t -test with * $P \leq 0.05$ and **** $P \leq 0.0001$.

167x86mm (200 x 200 DPI)

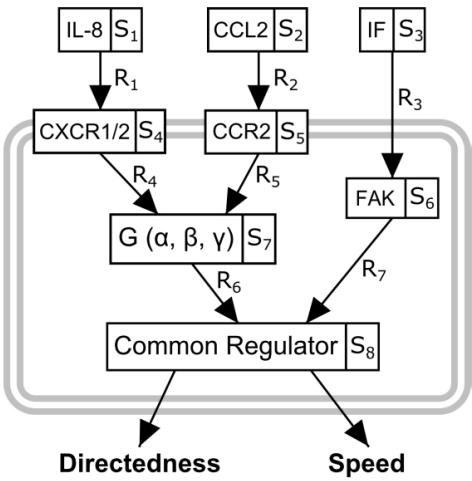


Figure 4. Hypothesized signaling model showing how signals associated with IL-8, CCL2 and interstitial flow (IF) activate a common regulator, both individually and in combination, to regulate macrophage migration directedness and speed. The input stimuli (IL-8, CCL2 and IF), associated cytokine receptors (CXCR1/2 and CCR2) and intermediary signaling species (*S1-S8*), including focal adhesion kinase (FAK) and heterotrimeric small G-proteins, G(α, β, γ), are identified by their respective abbreviations and species variables (Table 1 and Eq. 2-10 in section 'Mathematical model development'). These elements contribute toward interconnected signalling pathway reactions (reaction numbers *R1-R7*).

152x84mm (200 x 200 DPI)

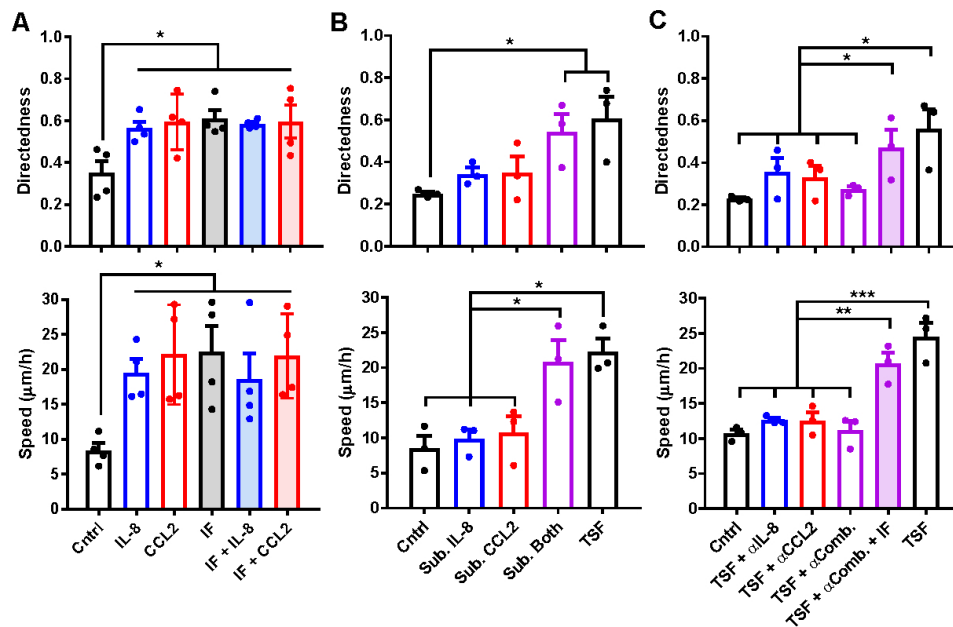


Figure 5. Directedness (top panel) and speed (bottom panel) of macrophage migration with the exogenous addition of a (A) saturating concentration (100 ng/mL) of IL-8 or CCL2 to a macrophage monoculture in the presence or absence of IF, or (B) sub-saturating concentration (25 ng/mL) of IL-8 and/or CCL2 to a macrophage monoculture, or the addition of (C) blocking antibodies against IL-8 and/or CCL2 to a macrophage-tumor cell co-culture in the presence or absence of IF. Data are shown as the mean \pm SEM ($n \geq 3$), where statistical significance was determined using a one-way ANOVA with Holm-Sidak's multiple comparisons test with * $P \leq 0.05$, ** $P \leq 0.01$, and *** $P \leq 0.001$. (Cntrl: control, IF: interstitial flow, Sub.: sub-saturating, Sub. Both: combined addition of sub-saturating concentrations of IL-8 and CCL2, TSF: tumor-secreted factors, α Comb.: combined blockade of IL-8 and CCL2)

161x106mm (200 x 200 DPI)

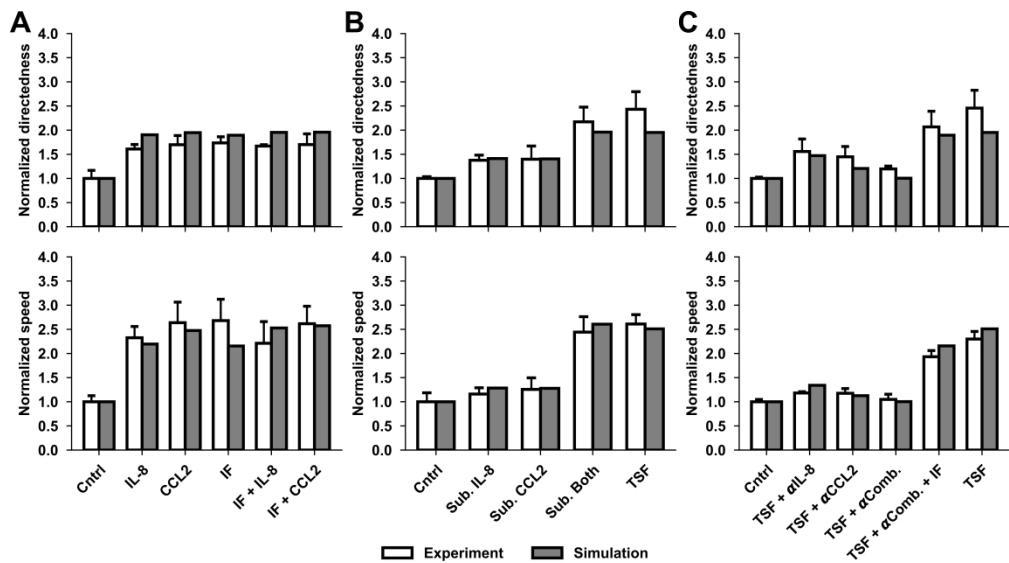


Figure 6. Comparison between *in vitro* experimental data (white) and model simulations (grey) of normalized macrophage migration directedness (top panel) and speed (bottom panel) with the exogenous addition of a (A) saturating concentration (100 ng/mL) of IL-8 or CCL2 to a macrophage monoculture in the presence or absence of IF, or (B) sub-saturating concentration (25 ng/mL) of IL-8 and/or CCL2 to a macrophage monoculture, or the addition of (C) blocking antibodies against IL-8 and/or CCL2 to a macrophage-tumor cell co-culture in the presence or absence of IF (100% antibody blockade of cytokines assumed). Data are shown as the mean \pm SEM ($n \geq 3$). The coefficient of determination (R^2) values were used to quantify the agreement between the simulated data and *in vitro* experimental data. (Cntl: control, IF: interstitial flow, Sub.: sub-saturating, Sub. Both: combined addition of sub-saturating concentrations of IL-8 and CCL2, TSF: tumor-secreted factors, α Comb.: combined blockade of IL-8 and CCL2).

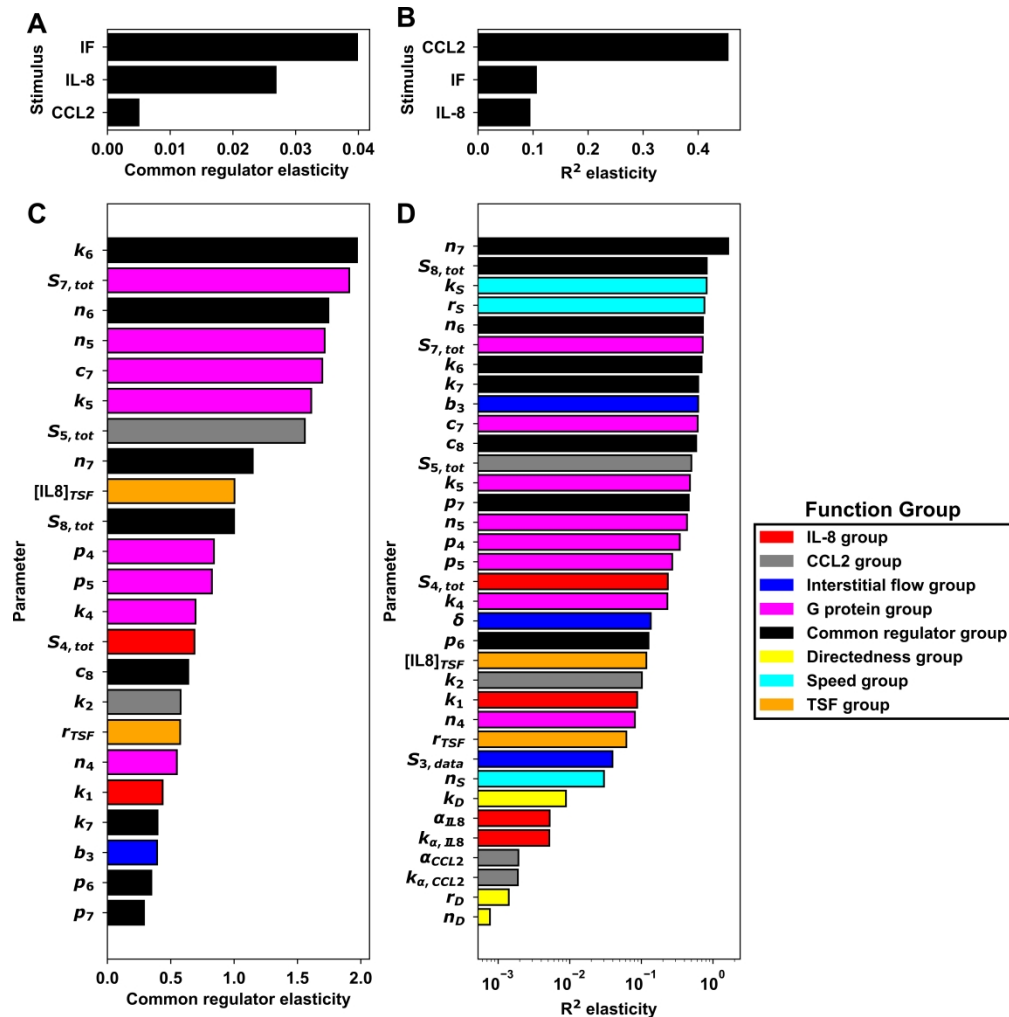


Figure 7. Sensitivity analysis that quantifies most influential stimuli and parameters on migration directedness and speed. The analysis considered (A) common regulator activation elasticity (Eq. 15) or (B) coefficient of determination (R^2) elasticity (Eq. 16) in response to varying the magnitude of each extracellular stimulus. Also considered was (C) common regulator activation elasticity (Eq. 17) or (D) R^2 elasticity (Eq. 18) in response to varying the magnitude of each parameter. The denominators $\Delta\%X$ and $\Delta\%P$ respectively represent a 20% change in the stimulus or the parameter under study. The numerator $\Delta\%[\text{Common Reg.}]$ and $\Delta\%R^2$ respectively represent the resulting percent change in concentration of active common regulator or the R^2 value between the model simulations and the *in vitro* experimental data. (A-C) are plotted on a linear x-axis. (D) is plotted on a base-10 logarithmic x-axis.

Supplementary Material

Integrated *in silico* and 3D *in vitro* model of macrophage migration in response to physical and chemical factors in the tumor microenvironment

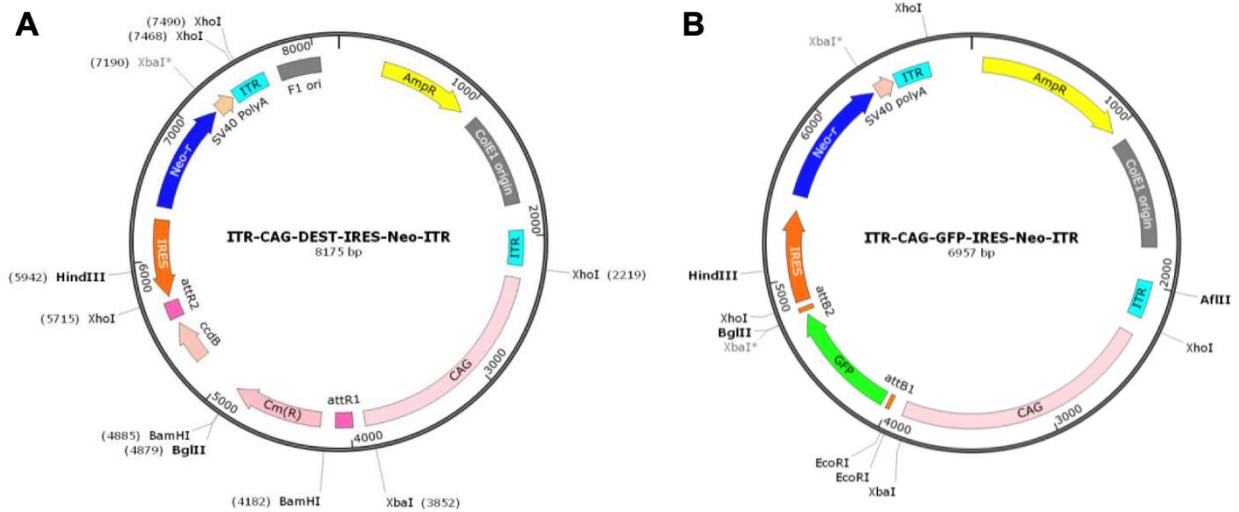
Lee, Sharon Wei Ling^{1,2,3,+}, Seager, R.J.^{4,+}, Litvak, Felix⁴, Spill, Fabian^{4,5,6}, Sieow, Je Lin³, Penny, Hweixian Leong³, Kumar, Dillip³, Tan, Alrina Shin Min³, Wong, Siew Cheng^{2,3}, Adriani, Giulia^{3,*}, Zaman, Muhammad Hamid^{4,7,*}, Kamm, Roger Dale^{5,8,*}

- ¹ BioSystems and Micromechanics IRG, Singapore-MIT Alliance for Research and Technology, Singapore, 138602, Singapore
- ² Department of Microbiology and Immunology, Yong Loo Lin School of Medicine, National University of Singapore (NUS), Singapore, 117597, Singapore
- ³ Singapore Immunology Network (SIgN), Agency for Science, Technology, and Research (A*STAR), Singapore
- ⁴ Department of Biomedical Engineering, Boston University, Boston, MA, 02215, USA
- ⁵ Department of Mechanical Engineering, Massachusetts Institute of Technology, Cambridge, MA, 02139, USA
- ⁶ School of Mathematics, University of Birmingham, Birmingham, B15 2TT, UK
- ⁷ Howard Hughes Medical Institute, Boston University, Boston, MA, 02215, USA
- ⁸ Department of Biological Engineering, Massachusetts Institute of Technology, Cambridge, MA, 02139, USA

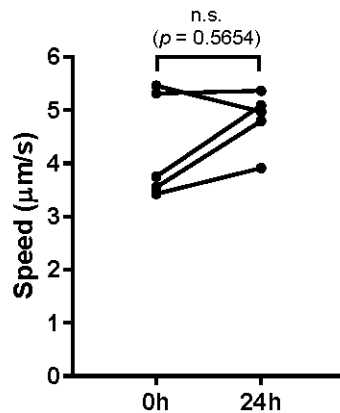
+ These authors contributed equally to the work.

* Corresponding authors.

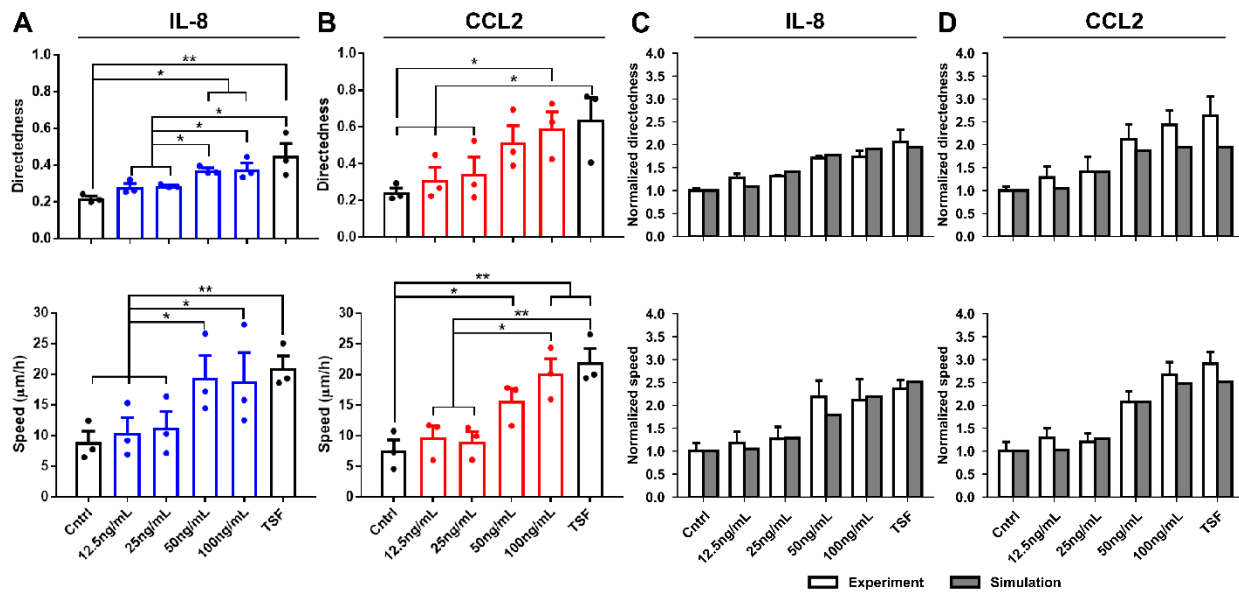
Roger Dale Kamm, Email: rdkamm@mit.edu
Muhammed Hamid Zaman, Email: zaman@bu.edu
Giulia Adriani, Email: giulia_adriani@immunol.a-star.edu.sg



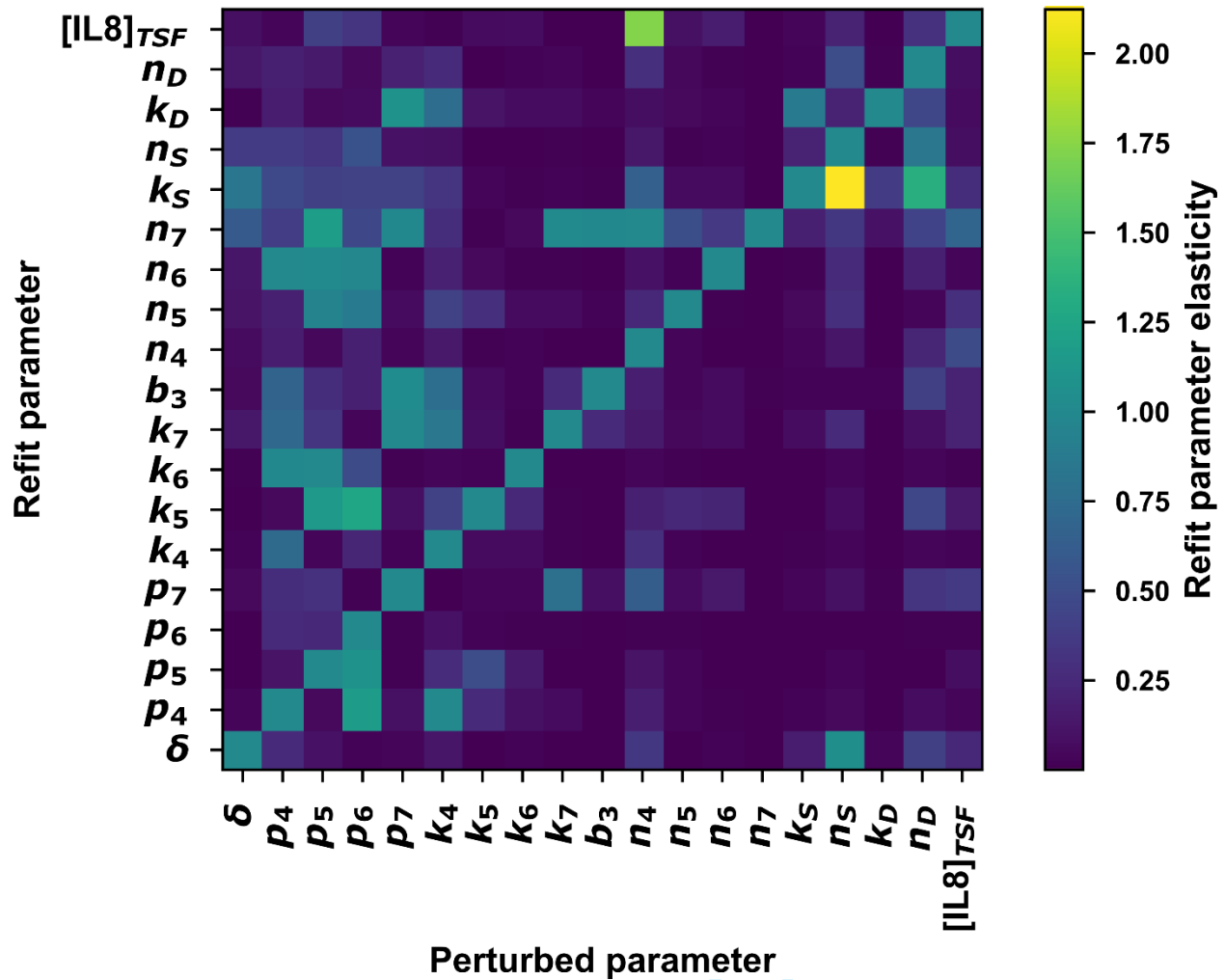
Supplementary Figure S1. For generation of GFP-tagged cell lines, SB100X-mediated transposition compatible plasmids were used as shown in (A) ITR-CAG-DEST-IRES-Neo-ITR (control plasmid) or (B) ITR-CAG-GFP-IRES-Neo-ITR (DEST cassette was replaced by GFP [PE1A-GFP] through LR gateway). Both plasmids are similar except for the GFP segment.



Supplementary Figure S2. Fluorescence recovery after photobleaching (FRAP) analysis of flow velocities within the gel of the 3D *in vitro* microfluidic model of interstitial flow (IF). Mean flow velocities at the start and end of the 24 h of IF treatment are shown. Velocities fall within 3-5 μm/s which correspond with physiological values of tumour IF. Data are shown as the mean (n = 5), with lines drawn to link the data points obtained at 0 h and 24 h timepoints in each experiment. Statistical significance was determined using a Student's *t*-test with $P \leq 0.05$ taken as evidence of a statistically significant difference. (n.s.: not significant)



Supplementary Figure S3. Macrophage migration directedness (top panel) and speed (bottom panel) in response to different concentrations of (A) IL-8 or (B) CCL2 that were added to a macrophage monoculture in the absence of interstitial flow. Comparison between *in vitro* experimental data (white) and model simulations (grey) of normalized directedness and speed of macrophage migration for the titration of (C) IL-8 or (D) CCL2. Data are shown as the mean \pm SEM ($n = 3$), where statistical significance was determined using a one-way ANOVA with Holm-Sidak's multiple comparisons test with * $P \leq 0.05$ and ** $P \leq 0.01$ (A, B). The coefficient of determination (R^2) values were used to quantify the agreement between the simulated data and *in vitro* experimental data (C, D). (Cntrl: control, TSF: tumor-secreted factors)



Supplementary Figure S4. Refit parameter elasticities for all free parameters. The ability of free parameters to compensate for changes in other free parameters was quantified by calculating a refit parameter elasticity that was computed for each free parameter according to (Eq. S1):

$$\phi_{Y,X} = \frac{\Delta\%Y}{\Delta\%X} = \frac{X_0 Y_{+10\%} - Y_{-10\%}}{Y_0 X_{+10\%} - X_{-10\%}} \quad (S1)$$

where the denominator represents a 20% change in free parameter X (centered at the default parameter value given in Table 2), the numerator represents the percent change in the value of a free parameter Y after a refit of the model to the *in vitro* experimental data, holding the perturbed value of X constant, X_0 and Y_0 are the default values of parameters X and Y , respectively, $X_{+10\%}$ and $X_{-10\%}$ are parameter X increased or decreased by 10%, respectively, and $Y_{+10\%}$ and $Y_{-10\%}$ are the values of free parameter Y obtained when

the 10% increase or decrease, respectively, to parameter X is held constant and the model is refit. This analysis gives additional context into the relationship between the various free parameters employed in the model. The heatmap shows all pairwise combinations of free parameters, indicating the degree to which each free parameter changes in response to a change in the value of one of the other free parameters, and a subsequent model refit against the *in vitro* experimental data.

For Review Only